Energy exchanges in Saturn's polar regions from Cassini observations: Part I: Eddy-zonal flow interactions

Peter L Read[1,1], Arrate Antuñano[2,2], Greg Colyer[3,3], Simon Cabanes[4,4], Teresa del Rio-Gaztelurrutia[5,5], and Agustín Sánchez-Lavega[6,6]

[1]Oxford University
[2]University of Leicester
[3]University of Oxford
[4]DICEA, Sapienza Università di Roma, Via Eudossiana 18, 00184 Rome, Italy.
[5]Universidad País Vasco UPV/EHU
[6]Universidad del Pais Vasco UPV/EHU

November 30, 2022

Abstract

Saturn's polar regions (polewards of ˜63° planetocentric latitude) are strongly dynamically active with zonal jets, polar cyclones and the intriguing north polar hexagon wave. Here we analyse measurements of horizontal winds, previously obtained from Cassini images by Antuñano et al. (2015), to determine the spatial and spectral exchanges of kinetic energy (KE) between zonal jets and eddies in Saturn's polar regions. As previously found for lower latitudes on Saturn, eddies of most resolved scales generally feed KE into the eastward and westward zonal jets at mean rates between 4.4×10^{-5} and 1.7×10^{-4} W kg^{-1}. In particular, the north polar jet (at 76oN) was being energised at a rate of ˜10^{-4} W kg^{-1}, dominated by the contribution due to the zonal wavenumber m=6 north polar hexagon wave itself. This implies that the hexagon was not driven through a barotropic instability of the north polar jet, but may suggest a significant role for baroclinic instabilities or other internal energy sources for this feature. The south polar jet KE was also being sustained by exchanges from eddies in that latitude band across a wide range of m. In contrast, results indicate that the north polar vortex may have been barotropically unstable at this time with eddies of low m gaining KE at the expense of the axisymmetric cyclone. However, the southern polar cyclone was gaining KE from the non-axisymmetric eddies at this time, including m=2 and its harmonics, as the elliptical distortion of the vortex may have been decaying.

Energy exchanges in Saturn's polar regions from Cassini observations: Eddy-zonal flow interactions

Peter L. Read[1], Arrate Antuñano[2,3], Simon Cabanes[4], Greg Colyer[1], Teresa del Río Gaztelurrutia[3], and Agustin Sanchez-Lavega[3]

[1]Atmospheric, Oceanic and Planetary Physics, Department of Physics, University of Oxford, Clarendon Laboratory, Parks Road, Oxford, OX1 3PU, UK
[2]School of Physics and Astronomy, University of Leicester, University Road, Leicester, LE1 7RH, UK
[3]Dpto de Física Aplicada, Escuela de Ingeniería de Bilbao, UPV/EHU, Spain
[4]DICEA, Sapienza Università di Roma, Via Eudossiana, 18 - 00184, Rome, Italy

Key Points:

- Wind velocities obtained from Cassini images are analysed to determine eddy-zonal mean exchanges of kinetic energy in Saturn's polar regions.
- Both the North and South Polar zonal mean jets at 76°N and 70°S are energised from non-zonal eddies, including the $m = 6$ NP Hexagon wave.
- The North Polar Vortex was barotropicallly unstable at this time, but the South Polar Vortex was gaining net kinetic energy from eddies.

Corresponding author: Peter L. Read, peter.read@physics.ox.ac.uk

Abstract

Saturn's polar regions (polewards of $\sim 63°$ planetocentric latitude) are strongly dynamically active with zonal jets, polar cyclones and the intriguing north polar hexagon wave. Here we analyse measurements of horizontal winds, previously obtained from Cassini images by Antuñano et al. (2015), to determine the spatial and spectral exchanges of kinetic energy (KE) between zonal mean zonal jets and nonaxisymmetric eddies in Saturn's polar regions. Eddies of most resolved scales generally feed KE into the eastward and westward zonal mean jets at rates between 4.3×10^{-5} and 1.4×10^{-4} W kg^{-1}. In particular, the north polar jet (at 76°N) was being energised at a rate of $\sim 10^{-4}$ W kg^{-1}, dominated by the contribution due to the zonal wavenumber $m = 6$ north polar hexagon wave itself. This implies that the hexagon was not being driven at this time through a barotropic instability of the north polar jet, but may suggest a significant role for baroclinic instabilities, convection or other internal energy sources for this feature. The south polar zonal mean jet KE was also being sustained by eddies in that latitude band across a wide range of m. In contrast, results indicate that the north polar vortex may have been weakly barotropically unstable at this time with eddies of low m gaining KE at the expense of the axisymmetric cyclone. However, the southern axisymmetric polar cyclone was gaining KE from non-axisymmetric components at this time, including $m = 2$ and its harmonics, as the elliptical distortion of the vortex may have been decaying.

Plain Language Summary

Saturn's polar regions (polewards of $\sim 63°$ latitude) are strongly meteorologically active with high speed eastward zonal jets (at 76°N and 70°S), intense, hurricane-like polar cyclones and the intriguing north polar hexagon wave (at 76°N). Here we analyse measurements of horizontal winds, previously obtained by tracking features in images from the Cassini Orbiter spacecraft, to determine how kinetic energy is exchanged between the longitudinally averaged zonal jets and various types of nonaxisymmetric eddy. As measured previously at low- and mid-latitudes on Jupiter and Saturn, we found that Saturn's 76°N and 70°S jets were gaining energy at the expense of nonaxisymmetric waves and eddies, including the northern polar hexagonal meanders, suggesting an important energetic role for heat transporting processes in Saturn's circulation. Energy exchanges within the polar vortices themselves were more complicated, with the suggestion that asymmetric distortions of the circular vortices (evident in high resolution images) were either growing or decaying at the time of observation.

1 Introduction

Since the Cassini orbiter mission to Saturn, it has been clear (Sánchez-Lavega et al., 2006; Dyudina et al., 2008, 2009; Baines et al., 2009; Antuñano et al., 2015; Sayanagi et al., 2017, 2018) that its polar regions are dominated at the cloud-top levels by intense, cyclonic vortices, centred on each pole, surrounded by an additional eastward jet stream at latitude 70° S and 76° N respectively (planetocentric); see Figure 1. The polar vortices in both hemispheres extend to a radius of around 5° colatitude, corresponding to around 4700 km (Sánchez-Lavega et al., 2006; Sayanagi et al., 2017; Liu et al., 2019), with strong circumpolar jets peaking at around 87° latitude with velocities of up to 160 - 175 m s^{-1}. The vortices appear to be roughly circular, with spiral cloud bands and an apparent clearing at the centre of each vortex, reminiscent of terrestrial tropical cyclones. But high resolution images (Sánchez-Lavega et al., 2006; Dyudina et al., 2008, 2009; Baines et al., 2009; Sayanagi et al., 2017; Liu et al., 2019) indicate many small-scale cloudy features that break the circular symmetry.

Weak westward zonal flow is found immediately beyond the edge of each polar vortex, reversing at lower latitudes to form the secondary eastward circumpolar jets in the zonal mean (South Polar Jet and North Polar Jet; SPJ and NPJ) at approximately 70°

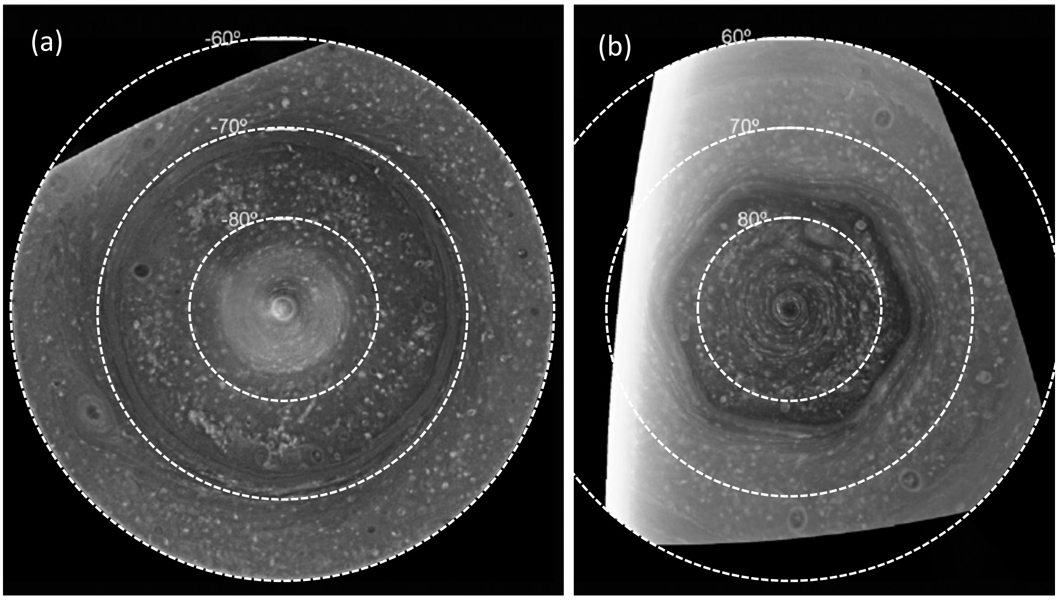

Figure 1: (a) Polar projection of the south polar region from 60° to 90°S, built using four different images captured by the Cassini ISS wide-angle camera with a CB2 filter on 3 December 2008. (b) An equivalent projection of the north polar region from 60° to 90°S, also from a Cassini wide-angle camera image obtained with a CB2 filter on 14 June 2013 (adapted from Antuñano et al. (2015), their Figure 1, with permission).

and 76° planetocentric latitude in the southern and northern hemispheres respectively (note that all latitudes in this paper are planetocentric) before reversing again at even lower latitudes. The NPJ is notable for its regular hexagonal shape, first discovered in Voyager images by Godfrey (1988). This North Polar Hexagon (NPH) feature has evidently persisted to the present day, and was observed in detail by the Cassini orbiter (e.g. Baines et al., 2009; Fletcher et al., 2018) in both cloud motions and in the retrievals of temperature in the lower stratosphere from Cassini Composite Infrared Radiometer (CIRS) measurements. Such a polygonal perturbation to the jet is not seen in the SPJ (Sánchez-Lavega et al., 2002), however, for reasons that are still poorly understood.

Indeed the nature and origin of both the polar cyclones and the NPH meanders continues to pose major challenges to atmospheric scientists (see Sayanagi et al., 2018, for a recent review), prompting a continuing need for more observational information with which to constrain theories and models. The resemblance of the polar vortices to terrestrial hurricanes, for example, would suggest a need for localised heating e.g. produced by latent heat release in moist convection (e.g. O'Neill et al., 2015, 2016; Sayanagi et al., 2017). But the compact morphology of terrestrial tropical cyclones is due in part to concentrated convergence and upwelling in the atmosphere associated with the underlying ocean surface (e.g. Montgomery & Smith, 2017), which is likely absent on Saturn.

The NPH has been the subject of much discussion since its discovery, not least because of its remarkable symmetry and stable persistence over several decades. Initial studies noted a possible association between the hexagon wave and a large anticyclonic vortex, known as the North Polar Spot (NPS), lying just outside the main jet at the time of the Voyager encounters (Godfrey, 1988), suggesting that the anticyclone was perturbing the circumpolar jet to induce a train of Rossby waves with a wavelength just matching the wavenumber $m = 6$ pattern at this latitude (Allison et al., 1990; Sánchez-Lavega et al., 1997). Subsequent observations from the Hubble Space Telescope showed that the

NPS persisted into the 1990s, but by the time the Cassini Orbiter arrived at Saturn it had disappeared. Cassini observations, however, showed that the NPH was still present even without the presence of the NPS, implying that the hexagon wave was not being maintained by the NPS.

More recent explanations proposed for the origin of the NPH attribute it either to a Rossby wave propagating upwards from a (nearly stationary) source in the deep interior (Sánchez-Lavega et al., 2014) or to an equilibrated instability (barotropic or baroclinic) of either a relatively shallow, initially axisymmetric NPJ itself (e.g. Aguiar et al., 2010; Morales-Juberías et al., 2011, 2015; Farrell & Ioannou, 2017; Rostami et al., 2017) or deep jets driven by deep planetary convection (Garcia et al., 2020; Yadav & Bloxham, 2020). The formation of polygonal jet flows as the fully developed form of either barotropic or baroclinic instabilities is well known in laboratory experiments (e.g. Hide & Mason, 1975; Sommeria et al., 1989, 1991; Bastin & Read, 1998; Früh & Read, 1999; Aguiar et al., 2010) though are much less commonly found in planetary atmospheres (however, cf Yadav & Bloxham, 2020). Equilibrated barotropic instabilities of plausible zonal jets were commonly found to be associated with chains of cyclonic or anticyclonic vortices alternately inside and outside of the meandering jet (Aguiar et al., 2010; Morales-Juberías et al., 2011; Yadav & Bloxham, 2020). Such vortex chains are not observed prominently on Saturn (Antuñano et al., 2015), though such features could conceivably be very weak or imperceptibile in some model parameter regimes with more complex vertical structure (e.g. Morales-Juberías et al., 2015). Baroclinic instabilities in stably-stratified flows may also lead to equilibrated meandering polygonal jet structures at certain levels in the vertical, with or without accompanying vortices (e.g. Bastin & Read, 1997, 1998). Such regimes may persist for as long as the initial jet is maintained. A plausible complete solution, for example, in which a jet is sustained by upscale kinetic energy transfers from small-scale eddies and develops a large-scale polygonal, meandering, wave-like barotropic instability, has been demonstrated in a two-layer numerical simulation by Farrell & Ioannou (2017). Such a "flux loop" mechanism emulates aspects of a similar scenario in two-dimensional stratified turbulence identified by Boffetta et al. (2011).

Observations have indicated that the maintenance of alternating jet flows on Saturn, at least at extra-tropical middle latitudes, is associated with strongly divergent or convergent Reynolds stresses that directly accelerate the zonal flow (Del Genio et al., 2007; Del Genio & Barbara, 2012) in a spectrally non-local transfer (i.e. direct from non-axisymmetric to zonal flow rather than via an incremental cascade) of kinetic energy (KE). This is similar to what has been found at mid-low latitudes in Jupiter's atmosphere, with an inferred mean transfer rate of $\sim\ 10^{-5} - 10^{-4}$ W kg^{-1} (Ingersoll et al., 1981; Sromovsky et al., 1982; Salyk et al., 2006). The sign and magnitude of the conversion rate of eddy kinetic energy at latitudes higher than $\pm 60°$ has not so far been determined (for either planet). Similarly, exchanges of kinetic energy between the NPH wave and other components of the flow have yet to be determined. Yet such statistics may shed important light on the nature of the NPH and other features at these high latitudes and provide important constraints on plausible models of these phenomena.

In the present work, therefore, we extend the analysis of the velocity field measurements of Antuñano et al. (2015) to explore the zonal kinetic energy spectra of both polar regions of Saturn and estimate the sign and magnitude of the rates of exchange of kinetic energy between the zonal mean jet flows and non-axisymmetric components of the flow (hereafter referred to as "eddies"). The data prove sufficient to obtain robust estimates of the total eddy-zonal mean conversion rate of KE for both polar regions and more locally in the vicinity of the SPJ, NPJ and both polar vortices. A zonal spectral decomposition of this conversion rate also allows a determination of the interaction between the $m = 6$ NPH meanders and the zonal mean NPJ and other features.

Section 2 summarises the observations used and the methods applied to obtain the KE spectra. Section 3 describes the methods used to compute the eddy-zonal KE con-

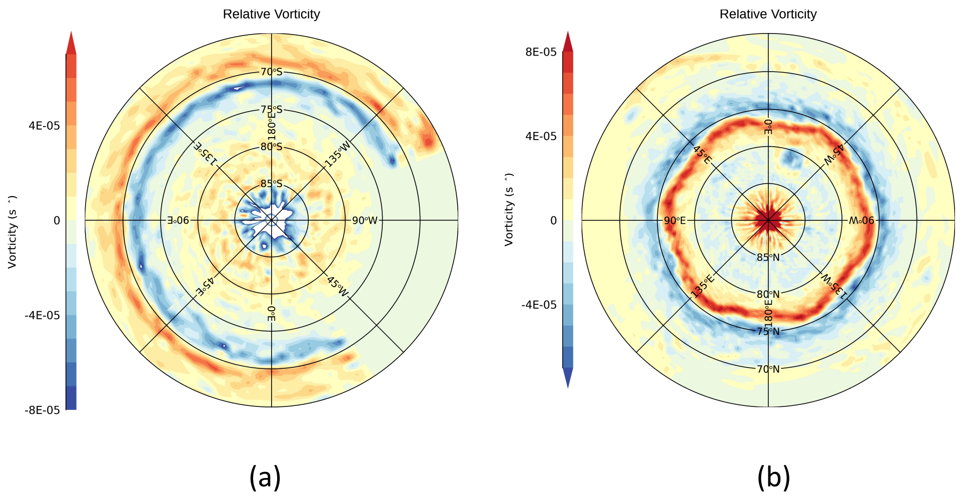

Figure 2: Cloud-top level vorticity fields, obtained from cloud-tracked wind measurements using Cassini ISS images by Antuñano et al. (2015), for Saturn's (a) south polar and (b) north polar regions. Note that the right hand rule is assumed, so red colours imply cyclonic vorticity in the northern hemisphere and anticyclonic in the south, and vice versa. Note also that velocity vectors were not available in the south equatorwards of 76°S between longitudes of ∼ 35°-110°W.

version rates and spectral and spatial fluxes. Section 4 presents the results on the eddy-zonal flow energy exchanges, including regional variations and their spectral decomposition.The results and their significance are discussed in Section 5 together with conclusions and suggestions for further work.

2 Observations

The observations used in the present study consist of two maps of horizontal velocities in Saturn's northern and southern hemispheres, as previously published by Antuñano et al. (2015). As fully described in that paper, these measurements were derived from sets of Cassini Imaging Sub-System (ISS) Wide Angle Camera (WAC) and Narrow Angle Camera (NAC) images using the continuum band CB2 and CB3 filters, acquired for the northern hemisphere in June 2013 and for the southern hemisphere using WAC CB2 and CB3 images taken in October 2006 and December 2008. Additional NAC images using the CB2 and red filters taken in July 2008 were also used to analyse the southern polar vortex. The WAC images covered a region extending from a planetocentric latitude of around 60-65° to each pole (apart from a segment in longitude between around 35° - 110°W) with a horizontal resolution equivalent to around 0.05° latitude (around 50km) per pixel, while NAC images were mostly used for the polar vortices, with a resolution equivalent to around 0.01° latitude (around 10 km) per pixel.

2.1 Velocity measurements

Horizontal velocities were obtained using semi-automated image correlation methods (i.e. involving some manual intervention, see Hueso et al., 2009; Sánchez-Lavega et al., 2019, for details) between pairs of images separated in time by intervals of approximately 1-10 hours. The correlation algorithm used pixel box sizes of 23×23 (in the north) or 25×25 (in the south), leading to a spatial resolution of the velocity vectors equivalent to around 1° latitude or 1000 km outside the polar vortices, reducing to around 0.2° or 200 km within the polar vortices themselves. The automatically generated velocity vectors were supplemented by a small number (around 1% of the total) of vectors obtained manually from the motion of visually identified cloud tracers. The estimated measurement uncertainty on each vector was around 5-10 m s^{-1}.

Figure 2 shows the maps of the relative vorticity in (a) the northern and (b) the southern hemispheres. These maps clearly show the regular, symmetrical North Polar Hexagon feature centred on the eastward jet at 76° N, the corresponding near-circular eastward jet centred at 71° S and the intense cyclonic polar vortices in each hemisphere. Zonal motion at intermediate latitudes is generally westward (relative to Saturn's System III; Desch & Kaiser (1981); Seidelmann et al. (2007); Archinal & et al. (2018)) but less strongly concentrated into clear jets. For the present study, the original velocity vectors from Antuñano et al. (2015) were interpolated onto a regular latitude-longitude grid using convex hulls and Delauney triangulation via the QHULL routine (Barber et al., 1996) of the Interactive Data Language (IDL). The final dataset was held on a grid separated by 3° (N) or 4° (S) in longitude and 0.23° (N) or 0.33° (S) in latitude. This almost certainly leads to some oversampling in latitude outside the polar vortices, so fields were typically smoothed to a latitudinal resolution of around 1° for some calculations. See the Supplementary Material for further information on the distribution of measured and interpolated velocity vectors and the raw velocity fields.

2.2 Errors and uncertainties

Sources of error and uncertainty in the velocity measurements were discussed by Antuñano et al. (2015). Principal sources of error considered were due to a combination of navigation uncertainties (uncertainties in locating and orienting each image used for correlation) and individual pixel errors. A number of different images were used to obtain these velocity measurements, including both wide and narrow angle cameras on the Cassini orbiter at various viewing and phase angles (see Antuñano et al., 2015, Table 2), so it is not straightforward to take into account differences in uncertainty in different locations. Navigation errors were estimated to be between 2 and 4 m s^{-1} in most cases, while pixel errors were estimated to be between 1 and 10 m s^{-1} from the effective horizontal resolution and time differences between image pairs. Navigation and pixel errors are expected to be uncorrelated and so here we combine these errors in quadrature and follow Antuñano et al. (2015) in estimating the effective uncertainty in individual velocity vectors to lie within the range 5-10 m s^{-1}. This does not, however, take account of the effects of interpolating onto a regular latitude-longitude grid.

Figure 3 shows profiles of the individual rms velocity components of u' and v', designated as $\delta u'$ and $\delta v'$, following subtraction of the zonal mean components $(\overline{u}, \overline{v})$. This clearly shows increases in both $\delta u'$ and $\delta v'$ in the vicinity of the north and south polar jets and the polar vortices, with $\delta u'$ typically somewhat greater than $\delta v'$ in these regions. Elsewhere, $\delta u'$ and $\delta v'$ take on background values where $\delta u' \simeq \delta v' \simeq 5-6$ m s^{-1}. We interpret this to suggest that the isotropic background fluctuations in u' and v' well away from major jets or polar vortices are dominated by measurement noise, suggesting nominal values of measurement error $\sigma_{u'} \simeq \sigma_{v'} \leq 6$ m s^{-1}. For the purposes of propagating velocity uncertainties into other derived quantities, therefore, hereafter we take 6 m s^{-1} to be the typical estimate of error in each velocity component.

2.3 Zonal mean velocities

The use of a regular latitude-longitude grid makes it easier, among other things, to compute zonal averages. Figure 4 shows profiles of the zonal mean zonal velocity $\overline{u}$

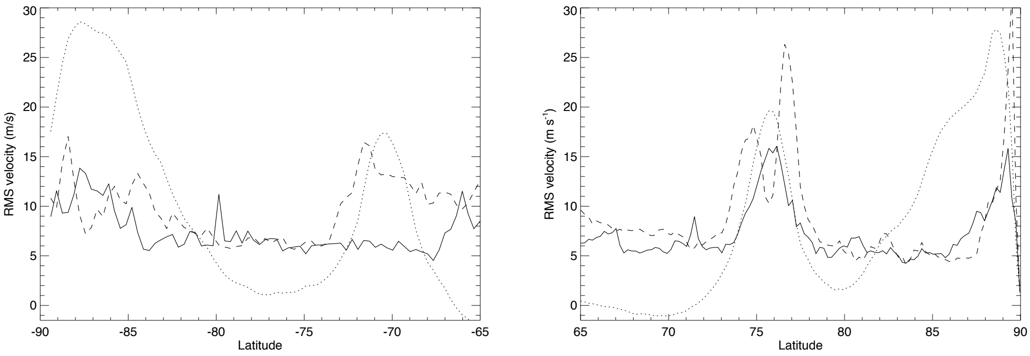

(a) (b)

Figure 3: Profiles of RMS values of u' (dashed lines) and v' (solid lines) for Saturn's (a) south and (b) north polar regions. Scaled profiles of the zonal mean wind $\overline{u}$ are shown dotted for reference.

in (a) the north and (b) the south, computed from the velocities on the new longitude-latitude grid. This clearly shows the strong eastward jets at 76° N and 71° S and the complex profile across the polar vortices. Both sets of jets are well resolved, with peak velocities of the North and South Polar Jets (NPJ and SPJ) around 100 and 80 m s^{-1} respectively. The zonal mean structure of the polar vortices indicates peak velocities of around 140 m s^{-1} in both hemispheres with complex "shoulders" on the equatorward side of each vortex that differ markedly between the north and south. This is slightly weaker in the south than shown by Antuñano et al. (2015) and Dyudina et al. (2009), likely due to some implicit smoothing in the interpolation used here to a somewhat lower resolution compared to the earlier studies.

2.4 Eddy kinetic energy

On subtracting the zonal mean velocities from the original velocity field, we can then calculate variances and covariances of the residual eddy components. Figure 5 shows the profiles of specific eddy kinetic energy (EKE) (neglecting any horizontal density variations), defined as

$$K_E = \frac{1}{2}(\overline{u'^2} + \overline{v'^2}), \tag{1}$$

as a function of latitude in each hemisphere, where primed quantities represent departures from the zonal mean (denoted by the overbar). This exhibits markedly different behaviour between each hemisphere, with much larger peak values of K_E in the north compared with the south. In particular, there is a pronounced double peak in K_E centred on the latitude of the NPJ, corresponding to the strong NPH hexagonal wave that modulates both u and v in longitude. An even stronger peak in K_E exceeding 500 m^2 s^{-2} is seen at the inner edge of the North Polar Vortex (hereafter NPV), indicating a strong departure of the vortex from a circular shape. Although a somewhat similar trend is seen with the south polar vortex it is much weaker ($<$ 200 m^2 s^{-2}) and more widely spread in latitude. These apparent peaks so close to each pole might be accentuated by

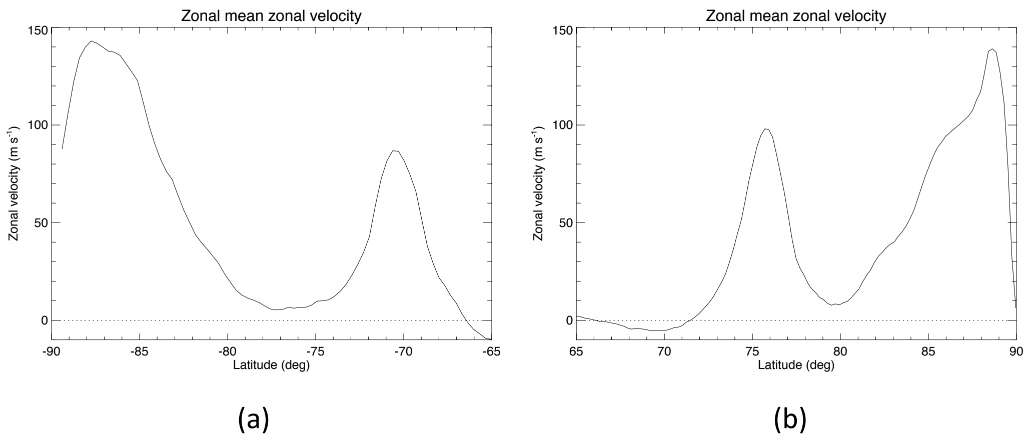

Figure 4: Zonal mean zonal velocity profiles, obtained from Cassini ISS images by Antuñano et al. (2015) and reinterpolated in the present work onto a regular longitude-latitude grid, for Saturn's (a) south polar and (b) north polar regions.

possible small systematic errors in location due to the interpolation method used here, although this is hard to quantify. There is also evidence for a weak and broad peak in K_E around the latitude of the SPJ but mostly < 100 m^2 s^{-2}. Despite these differences, the area-weighted average values of K_E in both hemispheres are remarkably similar (76.5 ± 0.8 J kg^{-1} in the north and 80.0 ± 0.8 J kg^{-1} in the south) and represent around 10% of the total horizontal kinetic energy in either hemisphere.

2.5 Eddy length scales

Given profiles of K_E we can then calculate estimates of quantities such as the Rhines wavelength scale λ_R, representing a cross-over scale between large-scale waves and small-scale turbulence (e.g. Vasavada & Showman, 2005; Chemke & Kaspi, 2015; Vallis, 2017) and defined in terms of K_E by

$$\lambda_R \simeq 2\pi \left(\frac{\sqrt{K_E}}{\beta} \right)^{1/2}, \tag{2}$$

where $\beta = (1/a) df/d\phi$ is the northward gradient of the Coriolis parameter, $f = 2\Omega \sin\phi$, with latitude ϕ. This typically represents a scale comparable to the distance between eastward or westward zonal jet maxima in geostrophic turbulence (e.g. Vasavada & Showman, 2005; Chemke & Kaspi, 2015; Vallis, 2017). This scale may also be compared with other length scales, such as Saturn's mean radius ($a = 5.823 \times 10^4$ km) and scales representative of energetic eddies, such as the first baroclinic Rossby radius of deformation, L_D. The latter is defined as a wavelength here by

$$\lambda_D = 2\pi L_D \simeq 2\pi \left(\frac{NH}{f} \right), \tag{3}$$

where N is the mean buoyancy or Brunt-Väisälä frequency, H is a vertical scale height (often taken somewhat arbitrarily to be the pressure scale height near 1 bar pressure). For Saturn, N is not well measured beneath the visible clouds though likely varies greatly

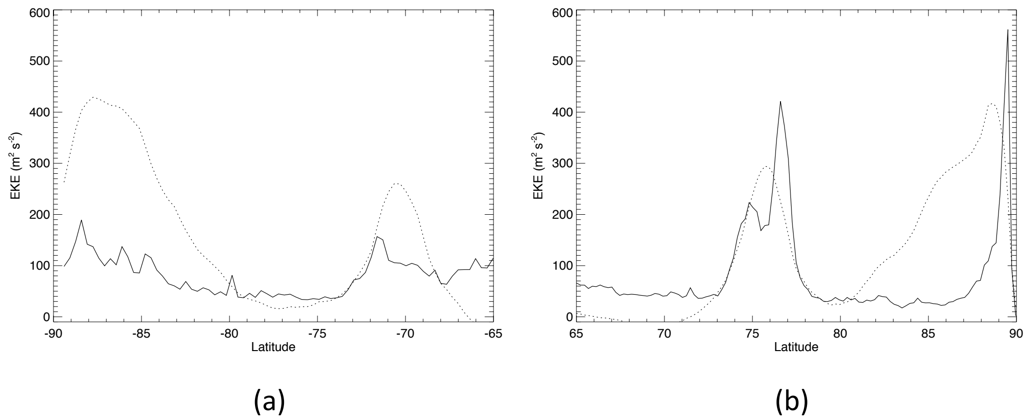

Figure 5: Profiles of EKE ($K_E = 1/2(\overline{u'^2 + v'^2})$) for Saturn's (a) south and (b) north (b) polar regions. Scaled profiles of the zonal mean wind $\overline{u}$ are shown dotted for reference.

with depth, and H is also not known with much confidence. L_D was estimated by Read et al. (2009) from measurements of Saturn's potential vorticity configuration near the cloud tops to vary approximately with latitude as $L_D \simeq 1500/\sin\phi$ km, so here we take

$$\lambda_D \simeq 3000\pi/|\sin\phi| \quad \text{km}. \tag{4}$$

Profiles of λ_R and λ_D, calculated using Eqs (2) and (4), are shown in Figure 6 for (a) the north and (b) the south. These show that both λ_R and λ_D are mostly much smaller than the planetary radius a and indicate how λ_R diverges to very large scales as each pole is approached (since $\beta \to 0$ as $|\phi| \to 90°$), while λ_D increases slowly with ϕ away from the pole. λ_R and λ_D are comparable around latitude $\phi \sim 60-65°$ in each hemisphere, indicating that λ_D may tend to be similar to or even larger than λ_R equatorward of around 60° (cf Chemke & Kaspi, 2015, their Fig. 4). There are local variations in λ_R, however, especially close to the NPJ, indicating that variations in λ_D/λ_R may be found elsewhere. But in general this suggests that Saturn's mid-high latitude regions are characterised by values of λ_D that are smaller than λ_R. It is also of interest to note that λ_R is comparable to the separation distance between the NPJ and SPJ and the adjacent eastward jets on the equatorward sides. λ_D at 76°N is around 10^4 km and corresponds to a longitudinal wavenumber of around $m = 9$ and is somewhat larger than the FWHM of the north polar hexagon at around 5800 km.

3 Analysis methods

In this section we outline the diagnostics used to examine the properties of the polar circulations on Saturn, with particular reference to the transfer of KE between different scales of motion.

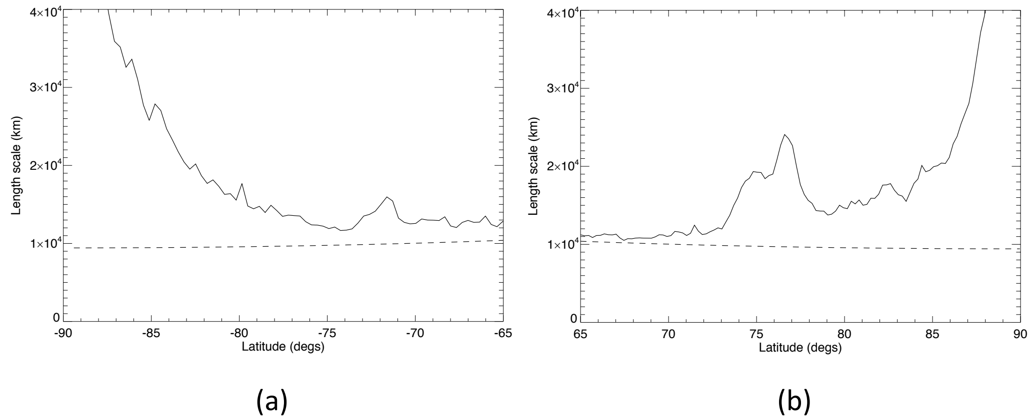

Figure 6: Key lengthscales computed for Saturn's south polar (a) and north polar regions (b). Solid line is the Rhines wavelength scale λ_R, while the dashed line shows estimates of the wavelength λ_D corresponding to the first baroclinic Rossby radius of deformation L_D (see text).

3.1 Eddy-zonal flow interactions

The forcing of zonal jets by eddies is commonly discussed in terms of the zonal mean zonal momentum equation, which can be written

$$\frac{\partial \overline{u}}{\partial t} - (f + \overline{\zeta})\overline{v} + \overline{w}\frac{\partial \overline{u}}{\partial z} = -\frac{1}{\rho_0}\nabla.\mathbf{F_m} + \overline{\mathcal{F}}, \tag{5}$$

(e.g. Andrews et al., 1987), where $\overline{\zeta}$ is the vertical component of zonal mean vorticity, $\overline{v}$ and $\overline{w}$ are the zonal mean meridional and vertical velocity components (where $\overline{v} > 0$ is northward in both hemispheres) and $\overline{\mathcal{F}}$ represents frictional effects and body forces acting on the flow. $\mathbf{F_m}$ represents the eddy flux of zonal momentum in the meridional (ϕ, z) plane due to the Reynolds stresses. In spherical coordinates, $\nabla.\mathbf{F_m}$ can be written

$$\frac{1}{\rho_0}\nabla.\mathbf{F_m} = -\frac{1}{a\cos^2\phi}\frac{\partial}{\partial\phi}(\overline{u'v'}\cos^2\phi) - \frac{1}{\rho_o}\frac{\partial}{\partial z}(\rho_0\overline{u'w'}). \tag{6}$$

where $\rho_0(z)$ is a background reference density profile, so $\mathbf{F_m}$ becomes

$$\mathbf{F_m} = -\rho_0\cos\phi[\overline{u'v'}, \overline{u'w'}]. \tag{7}$$

For the present problem we have no direct information on vertical velocity, other than to anticipate that it is likely to be much smaller than typical horizontal velocities (by a factor O($Ro.H/L$), where Ro is the Rossby number and H and L are vertical and horizontal lengthscales). So we will focus here on the horizontal eddy fluxes and the Reynolds stress divergence contribution to the energy budget.

The rate of conversion of kinetic energy between eddies and zonal mean flow is typically calculated from Eq (5), integrating in latitude (and height) across the domain. Neglecting the vertical dimension in the present context, we can calculate the rate of increase of zonal mean KE, denoted by K_Z as

$$\begin{aligned}\frac{dK_Z}{dt} &= C(K_E, K_Z) && (8)\\ &= -\frac{\int \left[\frac{\overline{u}}{a\cos\phi}\right] \frac{\partial}{\partial\phi}(\overline{u'v'}\cos^2\phi)d\phi}{\int \cos\phi d\phi} && (9)\\ &= \frac{\int \frac{\partial}{\partial\phi}\left[\frac{\overline{u}}{a\cos\phi}\right] \overline{u'v'}\cos^2\phi d\phi}{\int \cos\phi d\phi}, && (10)\end{aligned}$$

neglecting boundary terms in the usual way (cf Peixóto & Oort, 1974), where $C(K_E, K_Z)$ represents the corresponding conversion rate of eddy KE (K_E) to K_Z.

3.2 Errors and uncertainties in $\overline{u'v'}$ and $C(K_E, K_Z)$

Uncertainties in the values of $C(K_E, K_Z)$ determined via Eqs (9) or (10) are likely to be dominated by uncertainties in $\overline{u'v'}$ associated with velocity errors $\sigma_{u'}$ and $\sigma_{v'}$, which are relatively larger than those in $\overline{u}$ (cf Ingersoll et al., 1981). In estimating uncertainties in $\overline{u'v'}$ we follow Ingersoll et al. (1981), their Eq (7), assuming errors in u' and v' to be uncorrelated. Thus

$$\sigma^2(\overline{u'v'}) \simeq (\sigma_{u'}^2 \delta u'^2 + \sigma_{v'}^2 \delta u'^2 + \sigma_{u'}^2 \sigma_{v'}^2)/n, \tag{11}$$

where n is the number of velocity points in longitude used to calculate the momentum flux. This is an approximation since we assume $\delta u'$ and $\delta v'$ to represent the true signal even though they are actually contaminated by measurement noise. But this does at least provide an upper limit on the error in $\overline{u'v'}$ as $\sigma(\overline{u'v'})$.

For estimating uncertainty in the integrand of $C(K_E, K_Z)$ using Eq (10) (hereafter designated $c(K_E, K_Z)$), we follow Ingersoll et al. (1981) in neglecting the uncertainty in $d\overline{u}/dy = \cos\phi\ d/d\phi\,[\overline{u}/(a\cos\phi)]$ to obtain

$$\sigma(c(K_E, K_Z)) = \frac{\partial}{\partial\phi}\left[\frac{\overline{u}}{a\cos\phi}\right]\sigma(\overline{u'v'})\cos\phi, \tag{12}$$

for a particular latitude ϕ. The standard error in $C(K_E, K_Z)$, averaged over a range in latitude, is then given by

$$\sigma(C(K_E, K_Z)) = \frac{\int \frac{\partial}{\partial\phi}\left[\frac{\overline{u}}{a\cos\phi}\right]\sigma(\overline{u'v'})\cos^2\phi d\phi}{\sqrt{p}\int\cos\phi d\phi}, \tag{13}$$

where p is the number of latitude rows across the region of interest.

3.3 Spectral decomposition

The formulation above considers just the interaction between the zonal jet flow and non-axisymmetric eddies of all scales. The $C(K_E, K_Z)$ term can, however, be decomposed further into contributions from different zonal harmonics of wavenumber index m via a Fourier analysis of u' and v' in longitude (cf Chemke & Kaspi, 2015). Given the complex amplitude spectra of u' and v', denoted here by $\tilde{u'}$ and $\tilde{v'}$, the relevant self-interaction component of the Reynolds stress becomes

$$\widetilde{u'v'}(m,\phi) = \tilde{u'}(m,\phi)\tilde{v'}^*(m,\phi) + \tilde{u'}^*(m,\phi)\tilde{v'}(m,\phi), \tag{14}$$

where starred quantities represent complex conjugates. We can thus obtain the spectrally decomposed eddy-zonal KE conversion rate by extension of Eq (9) using Eq (14),

$$C(\widetilde{K_E, K_Z})(m) = \frac{\int \left[\frac{\overline{u}}{a\cos\phi}\right] \partial/\partial\phi(\widetilde{u'v'}(m,\phi)\cos^2\phi)d\phi}{\int\cos\phi d\phi}, \tag{15}$$

In our analyses below, therefore, we include computations of both $C(K_E, K_Z)$ and the integrand $c(\widetilde{K_E, K_Z})(m)$, integrated over various ranges in latitude and locally as a function of ϕ. Note that, for the southern hemisphere, the gap in longitude coverage of the wind measurements between 35° and 110° was filled by copying a segment of data from another interval in longitude. This was necessary to enable the use of Fast Fourier methods to compute zonal spectra. The sensitivity of quantities such as $c(\widetilde{K_E, K_Z})(m)$ to the range of longitudes used to fill the gap was evaluated by trying different longitude segments and found to be small compared with the estimated measurement uncertainties.

Uncertainties in $C(\widetilde{K_E, K_Z})(m)$ were estimated in a similar way to Eq (13), but in which the errors were spread with respect to wavenumber m assuming errors in each wavenumber were uncorrelated with every other. This is ensured by defining

$$\sigma^2(C(K_E, K_Z)) = \sum_m \sigma^2(C(\widetilde{K_E, K_Z})(m). \tag{16}$$

In the absence of more detailed information, we assume for simplicity that uncertainties are similar in magnitude at all scales, so the error estimate $\sigma(C(K_E, K_Z))$ is distributed evenly across all wavenumbers, even though it is likely, for example, that navigation errors are correlated on large scales whereas pixel errors are uncorrelated. It was not possible to track these errors in detail between different image pairs but readers should be aware that errors may actually be larger at small m than for higher wavenumbers.

4 Eddy-zonal flow interactions

In this section we present the results of analysing the rates of conversion between eddy and zonal mean KE in the vicinity of both polar regions of Saturn. Calculations include both the total conversion rate averaged over the whole polar region $|\phi| > 65°$ and particular subranges of ϕ to focus on both polar vortices and the NPJ and SPJ.

4.1 Total conversion rates

Given the gridded velocity fields described in Section 2 above, it is straightforward to compute the northward flux of eddy momentum, $\overline{u'v'}$, at each latitude row to obtain the profiles presented in Figure 7(a) and (b). The unfiltered/unsmoothed results are somewhat noisy, as is clear from the error estimates shown by the error bars in Figs 7(a) and (b), computed from Eq (11), and the correlation coefficients between u' and v'; see Fig. S4 in the Supplementary Material. But there are clear features, coherent in latitude, in the profiles at the locations of the south polar vortex and around the latitudes of the north and south polar jets. Fig. 7(a) and (b) also show dashed profiles of the zonal mean wind $\overline{u}$ (scaled by 1/5) in each hemisphere for reference. This shows some complex structure around the polar vortices, but with clear changes of sign of $\overline{u'v'}$ close to the cores of both the NPJ and SPJ.

Calculating nominal values of the integrand $c(K_E, K_Z)$ from Eq (10), without any explicit smoothing in latitude, we obtain the mean local KE conversion rate from eddies into the zonal jet, with the results shown in Figs 7(c) and (d). Error bars represent the estimated uncertainty according to Eq (12) and indicate clear regions of strong eddy-zonal flow interactions in the south polar vortex and on either side of the jet cores at 69°-73°S and 74°-78°N. The results indicate a significant positive conversion from eddies to zonal flow within the NPJ and SPJ, and also within the SPV polewards of 83°S. The pattern of $c(K_E, K_Z)$ in the NPV, however, looks more complicated and noisy, with no obvious direction of energy conversion.

Integrating these local conversion rates over the whole polar domain in each hemisphere using Eq (9), we obtain the overall mean conversion rates shown in the first two rows of Table 1. This shows a general trend for eddies to be transferring KE into the zonal

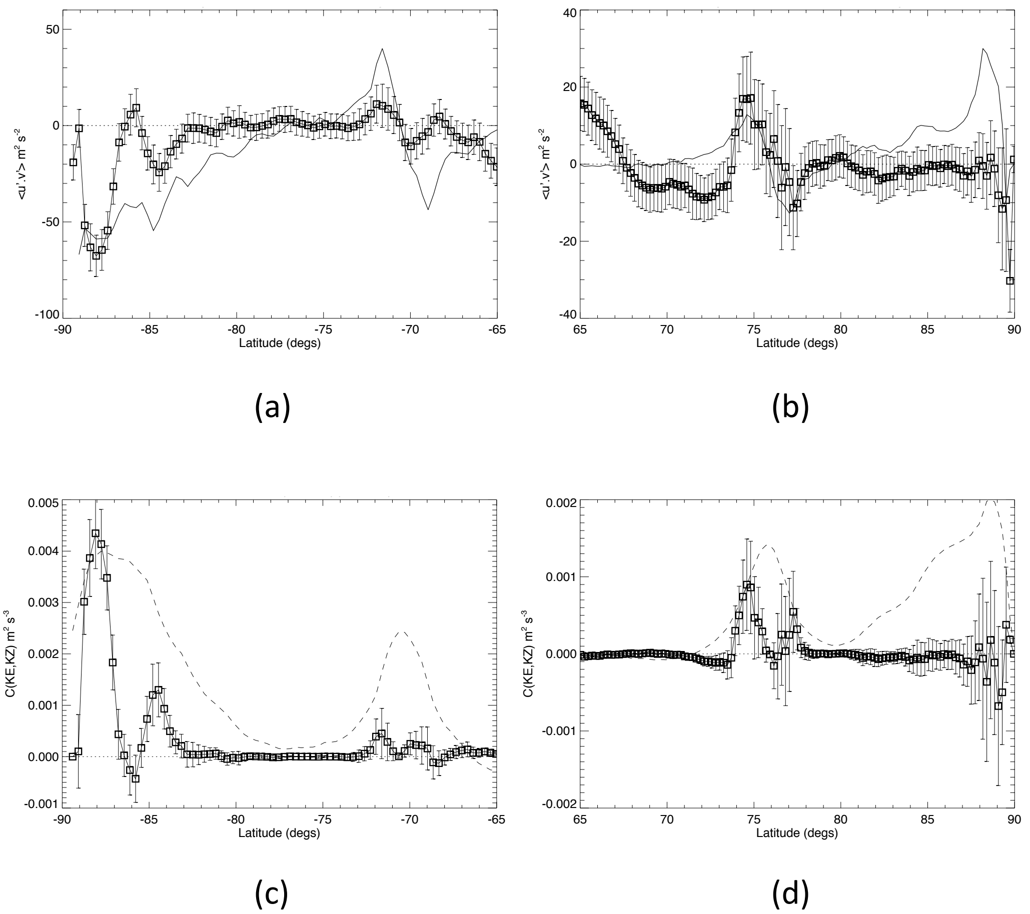

Figure 7: (a,b) Profiles of eddy momentum flux, $\overline{u'v'}$, smoothed in latitude to a resolution of 1° for Saturn's (a) south polar and (b) north polar regions. Dashed lines in (a) and (b) show the corresponding profiles of $d/d\phi(\overline{u}/\cos\phi)$ while scaled profiles of $\overline{u}$ are shown in (c) and (d) . Note that different scales are used for the axes in the plots in (a) and (b) to show the features more clearly. (c,d) Profiles of KE conversion rate $c(K_E, K_Z)$ as given by the integrand of Eq (10) for the southern (c) and northern (d) polar regions.

jets in both polar regions, though at around three times the rate in the south compared with the north, at least at the time when these observations were acquired. The uncertainties are estimated as discussed in Section 3.2, Eq (13).

Table 1: Eddy-zonal flow kinetic energy conversion rates on Saturn, computed over different latitude ranges using the area-weighted mean of the Lorenz form defined in Eq (10) and the local Reynolds stress divergence defined in Eq (9) from the dataset of Antuñano et al. (2015).

Feature	Latitude range (°)	$C(K_E, K_Z)$ (W kg^{-1})
North polar region	66° – 90°N	4.3 $\pm 2.3 \times 10^{-5}$
South polar region	66° – 90°S	1.4 $\pm 0.3 \times 10^{-4}$
North polar jet	70° – 79°N	1.0 $\pm 0.5 \times 10^{-4}$
South polar jet	66° – 76°S	8.7 $\pm 3.7 \times 10^{-5}$
North polar vortex	80° – 90°N	-4.2 $\pm$ 3.6 $\times 10^{-5}$
South polar vortex	80° – 90°S	4.7 $\pm 0.6 \times 10^{-4}$

4.2 Regional conversion rates

If we focus attention on particular features or regions, it is of interest to evaluate the contribution of the northern and southern polar jets and the polar vortices to the overall transfer of KE from eddies to zonal flow in each polar region. The juxtaposition of the peaks and troughs of $\overline{u'v'}$ in Fig. 7(a) and (b) with the profile of $\overline{u}/\cos\phi$ suggest a possible local correlation between $\overline{u'v'}$ and $d/d\phi(\overline{u}/\cos\phi)$, especially in the vicinity of the NPJ and SPJ, consistent with a positive contribution to $C(K_E, K_Z)$ (cf Eq (10)).

Also shown in Table 1 are the values of $C(K_E, K_Z)$ computed over latitude ranges centred respectively on the zonal mean polar jets and vortices. For the polar jets, centred respectively at around 76°N and 70°S, $C(K_E, K_Z)$ is strongly positive, indicating a relatively powerful local transfer of kinetic energy from eddies into each jet at a level of order 10^{-4} W kg^{-1}. For these features, the conversion rate into the NPJ is somewhat larger than in the SPJ and somewhat larger in the north than the average across the rest of the north polar region. This is in contrast to the south where the conversion rate into the SPJ is similar to or slightly less than the average across the south polar region. From this calculation, however, it is not clear which scale of nonzonal eddies or waves might be determining the overall rate of KE transfer into the zonal mean zonal jets. In particular, the role of the wavenumber $m = 6$ meanders in the north polar hexagon in these transfers is not clear since there are evidently waves of many differing zonal wavenumbers present across both regions.

For the polar vortices, the calculations of $C(K_E, K_Z)$ reveal major differences between the NPV and the South Polar Vortex (SPV), at least so far as their energetics are concerned. For the NPV, $C(K_E, K_Z)$ is seen in Table 1 to be small and negative with a value around $-4.2 \pm 3.6 \times 10^{-5}$ W kg^{-1}. This would suggest that eddies are gaining just a little KE at the expense of the zonally symmetric zonal flow in the vortex, perhaps marginally suggestive of a barotropic instability though with relatively large uncertainty. Such an instability would not be unduly surprising, for example, if such polar vortices were dynamically similar in some respects to the cores of tropical cyclones on Earth, leading to the growth of elliptical or even polygonal distortions of the main vortex. For the SPV, however, $C(K_E, K_Z)$ is seen in Table 1 to be strongly positive when

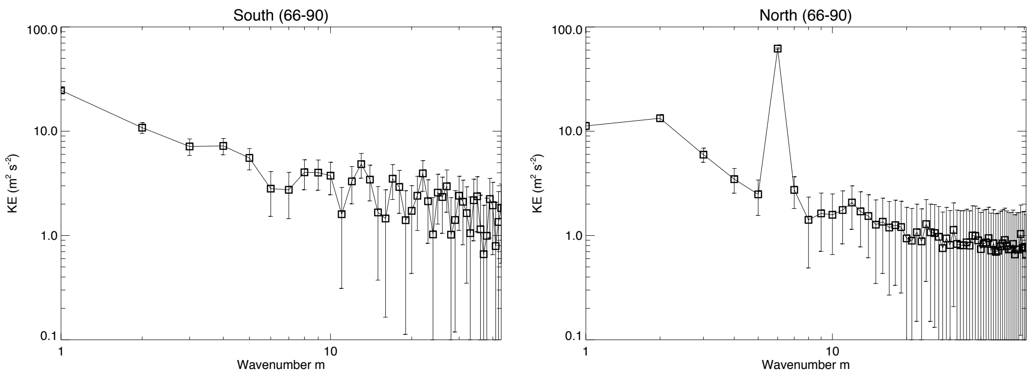

(a) (b)

Figure 8: Area-weighted kinetic energy spectra for (a) the southern and (b) the northern polar regions (66°–90° latitude). An alternative version of this figure with linear scales on the axes is presented as Figure S5 in the Supplementary Material.

integrated over the entire SPV poleward of 80°S with relatively high statistical significance. However, Fig. 7(a) indicates that the conversion rate varies a lot with latitude with strong convergence of eddy momentum fluxes near latitudes of 85° and 89°S and divergent fluxes (indicative of local westward forcing of zonal flow) around 87° and 84°S. This would seem to suggest that parts of the axisymmetric southern polar vortex were gaining energy from non-axisymmetric eddies while other parts of the vortex were losing energy, although more information, e.g. on the structure of flow, may be desirable to interpret this result.

4.3 Spectral decomposition

Although the simple partitioning of the flow between zonally symmetric and non-axisymmetric components allows us to determine the overall rate of KE conversion between eddies and zonal jets, this approach integrates over all eddy length scales. As a result it does not provide much insight into the roles of eddies of different lengthscales in either driving or feeding barotropically off of the zonal jets. As outlined in Section 3.1 above, however, we can further decompose the flow into its zonal harmonics and thereby examine the contribution of each zonal wavenumber to the overall energy budget for the zonal jets.

Although the north polar hexagon feature is prominent in the northern polar regions, the area-averaged zonal kinetic energy spectrum (see Figure 8(b)) shows that kinetic energy is present at all zonal wavenumbers that are resolved in the observations. Thus, we see in the north a sloping continuum in the spectrum of KE with increasing m, leading into a fairly clear noise floor (cf the estimated error bars) for $m \gtrsim 20$, upon which is superposed a strong peak at $m = 6$ representing the north polar hexagon. In the south, however, the spectrum appears flatter and somewhat weaker overall than in the north at low wavenumbers (see Fig. 8(a)) but still with significant EKE stretching to some higher wavenumbers above the noise floor of around 1-2 J kg^{-1} per wavenumber.

Decomposing $C(K_E, K_Z)$ into its zonal harmonics using Eq (15) we can quantify the contributions to the zonal mean KE budget due to different zonal wavenumber components. Figure 9 shows the integrand of the numerator of Eq (15),

$$c(\widetilde{K_E, K_Z})(m, \phi) = \left[\frac{\overline{u}}{a \cos^2 \phi}\right] \frac{\partial}{\partial \phi} \left(\widetilde{u'v'}(m, \phi) \cos^2 \phi\right), \tag{17}$$

as a function of both zonal wavenumber m and latitude ϕ for each of the north and south polar jets and polar vortices. $c(\widetilde{K_E, K_Z})(m, \phi)$ for the SPJ for shows a broadly positive local conversion of eddy to zonal KE over a wide range of zonal harmonics, centred on the jet core, with weaker negative conversions on the flanks of the zonal jet. In contrast, the equivalent local conversion of eddy KE into the NPJ is clearly dominated by the contribution from the $m = 6$ hexagonal wave (Fig. 9(a)), with a strong positive contribution into the jet core and weaker negative contributions on both its northern and southern flanks. This indicates clearly that the $m = 6$ component of the hexagon wave itself is feeding KE into the zonal mean NPJ, tending to accelerate its core and decelerating the flanks, thereby tending to sharpen the eastward jet. Contributions from other zonal harmonics are much weaker and more complicated in latitudinal structure, though a small signal at the first harmonic of the hexagon, $m = 12$, is evident among others with a weak dipolar structure in latitude.

The structure of the $m = 6$ component that leads to the upscale conversion of KE into the $m = 0$ zonal jet is shown in Figure 10, which presents the amplitude and phase profiles of u' and v' (Fig. 10(a) and (b)) and their net contribution to $\overline{u'v'}$ in Fig. 10(c). This clearly shows $v'(m = 6)$ peaking in amplitude around the zonal mean jet core while $u'(m = 6)$ has a double-peaked structure on the flanks of the zonal mean jet. The phase of $v'(m = 6)$ seems remarkably constant across the whole region while $u'(m = 6)$ jumps by approximately π at the jet core, consistent with a change of sign of u' on either side of the jet (for a rendering in physical space of the superposition of the $m = 0$ and $m = 6$ components of the velocity field, which accounts for more than 93% of the total kinetic energy between 72° and 80°N, see Figure S7 in the Supplementary Material). The contribution of $m = 6$ to $\overline{u'v'}$ is determined by the product of the amplitudes of u' and v' and the phase difference between them. Defining

$$u'(m) = U_6(\phi) \cos(m\theta + \gamma(\phi)) \tag{18}$$
$$v'(m) = V_6(\phi) \cos(m\theta), \tag{19}$$

where γ is the phase difference between u' and v', the contribution of the component m to $\overline{u'v'}$ is given by

$$\overline{u'v'}(m, \phi) = \frac{U_6(m, \phi) V_6(m, \phi)}{2} \cos(\gamma(m, \phi)). \tag{20}$$

The observed structure of the $m = 6$ component of the NPH shows a slight shift in phase difference between u' and v' such that $\cos(\gamma(m, \phi))$ is non-zero at most latitudes and changes sign across the zonal mean jet core (see Figure Fig. 10(c)).

Fig. 11 also shows the corresponding profile of $\overline{u'v'}(m = 6, \phi)$, which has a similar distribution to the total $\overline{u'v'}$ profile (shown as a dashed line) and evidently accounts for most of the total $\overline{u'v'}$ due to all resolved zonal harmonics.

$c(\widetilde{K_E, K_Z})(m, \phi)$ for the NPV is more complicated (see Fig. 9(d)) but is evidently dominated by contributions from low wavenumbers $m < 5$, particularly very close to the pole. The predominance of a strong contribution from $m = 1$ is somewhat surprising though images of the vortex (e.g. Antuñano et al., 2015; Sayanagi et al., 2017, and Fig. 9(a)) do appear to show some spiral cloud features and occasional secondary vortices that may break its circular symmetry. The significance of $m = 1$, however, might be indicative of a small displacement of the (nearly axiymmetric) vortex away from the assumed position of the pole. Figure 12(b) shows a Cassini ISS image of the NPV with

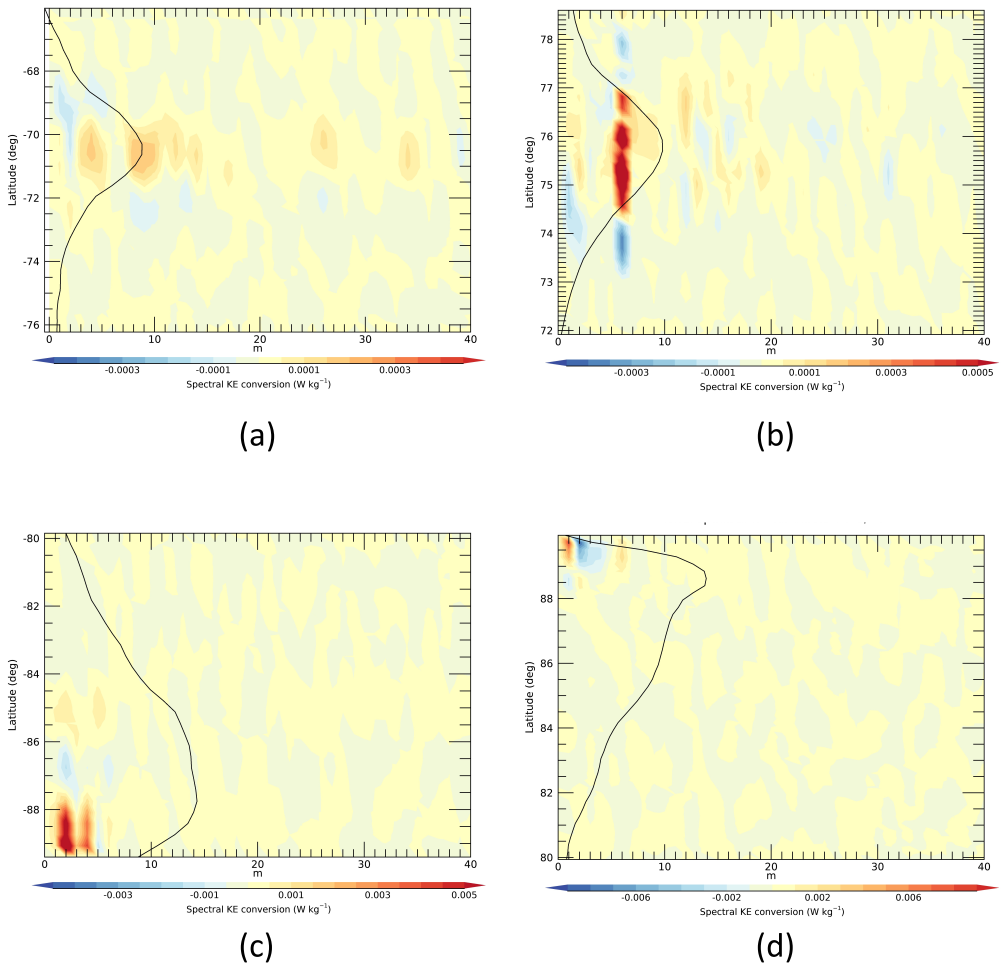

Figure 9: Spectrally resolved, local eddy-zonal flow KE conversion rate, given by Eq (17), $c(\widetilde{K_E, K_Z})(m, \phi)$, vs zonal wavenumber m and latitude ϕ, for (a) Saturn's south polar jet, (b) north polar jet, (c) south polar vortex and (d) north polar vortex. Note the difference in colour scales between each frame.

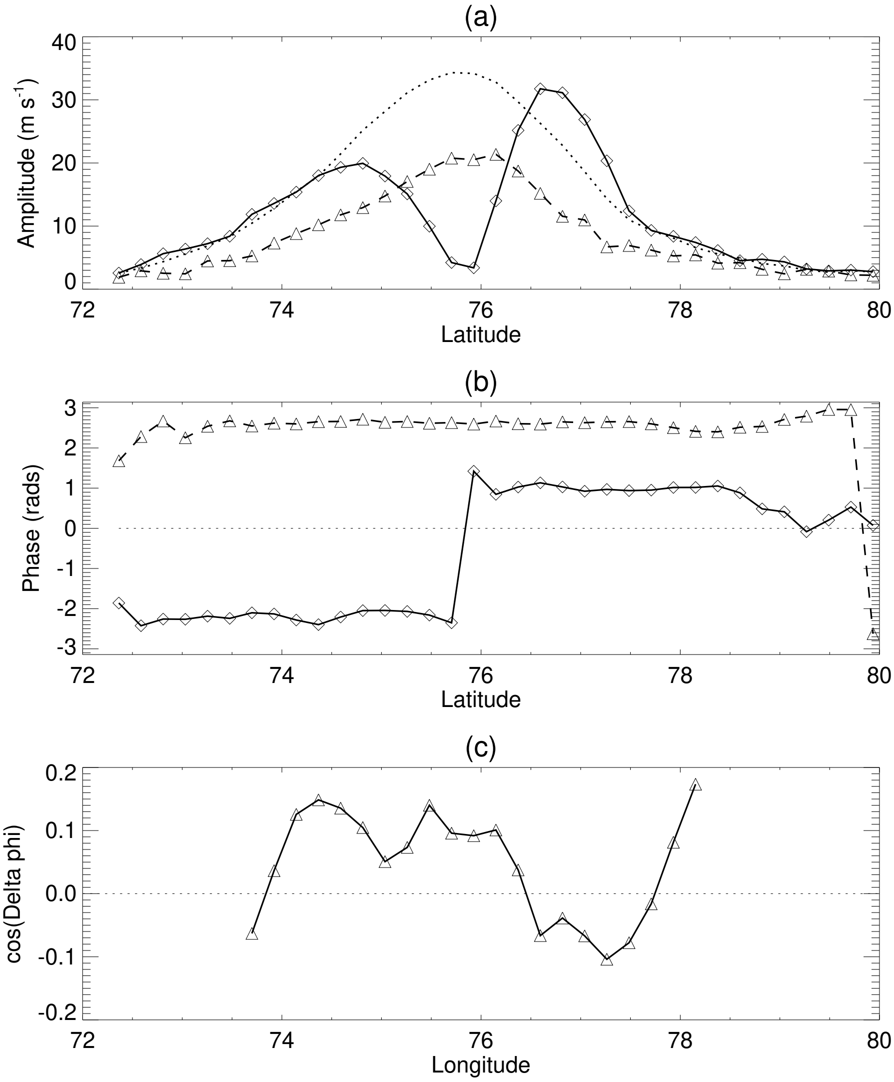

Figure 10: Latitudinal structure of the $m = 6$ component of the NPH from Fourier decomposition of the north polar wind fields. (a) amplitude profiles of u' (solid line with diamond points) and v' (dashed line with triangle points) together with scaled profile of the $m = 0$ (zonal mean $\overline{u}$; dotted line); (b) profiles of zonal phase of $m = 6$ for u' (solid line with diamond points) and v' (dashed line with triangle points); (c) profile of $\cos(\gamma(6, \phi))$, representing the cosine of the phase difference between the $m = 6$ components of u' and v' (cf Eq (20)).

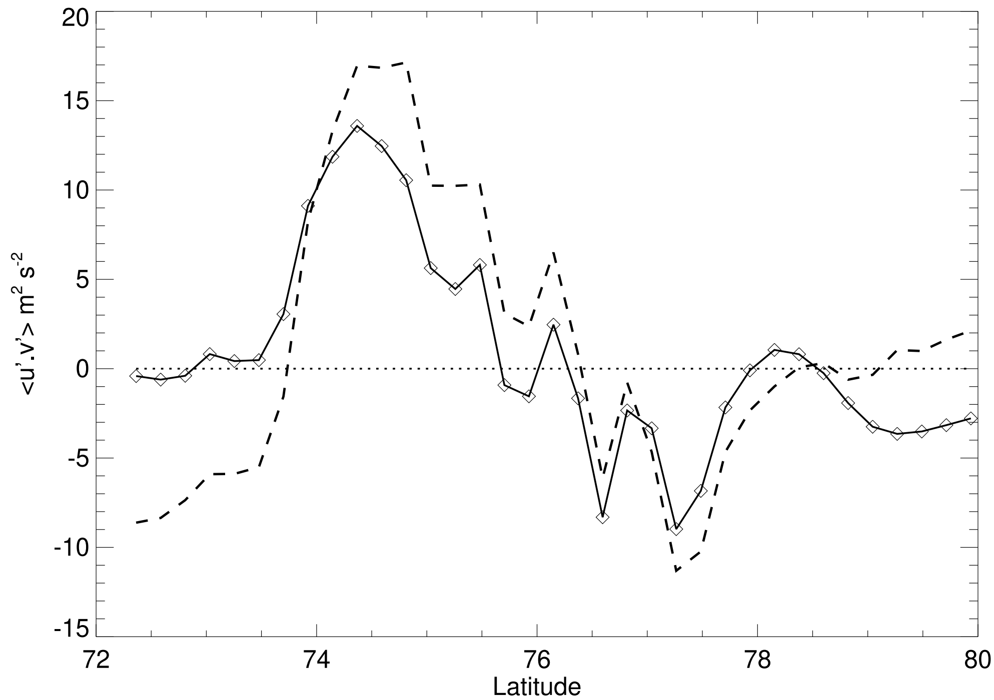

Figure 11: Latitudinal structure of the $m = 6$ contribution to $\overline{u'v'}$ (solid line with diamonds) in the vicinity of the NPH (cf Eq (20)) from the Cassini velocity measurements. The full profile of $\overline{u'v'}$ in this region is shown by the dashed line, indicating that $m = 6$ accounts for most of the meridional momentum flux at these latitudes.

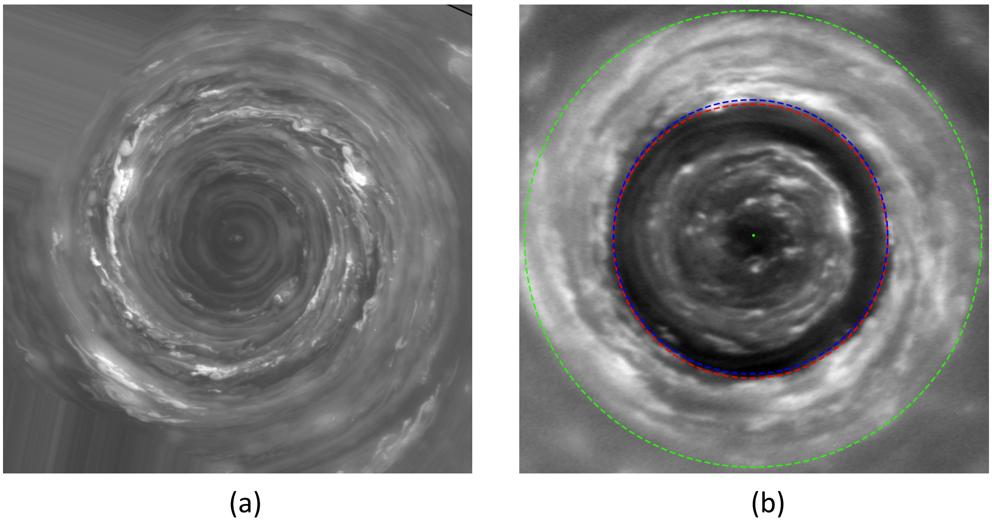

Figure 12: Images of the core of Saturn's North Polar Vortex, obtained by the Cassini ISS Narrow-angle camera using the CB2 filter in (a) June 2013 (Image N1749893515_1 (COISS 2083)) and (b) April 2014 (Image N1775155245_1 (COISS 2090)) using the Wide-angle camera. The image in (b) shows blue and green dashed circles centred on the best estimate of Saturn's north pole (at latitudes of 88.6° and 87.7° N respectively), while the (slightly displaced) red circle is aligned with the approximately circular cloud albedo boundary. Image scale of (a) is 5.3 km per pixel and of (b) is about 17 km per pixel. Image credits from NASA/JPL/Space Science Institute with permission.

blue and green dashed circles centred on the best estimate of the position of Saturn's north pole. The red dashed circle, however, is aligned with the approximately circular cloud albedo boundary and is slightly displaced from the nearby blue latitude circle, which may indicate either a small navigation error or an actual displacement of the NPV from the north pole itself. Other significant components at $m \geq 2$ would suggest a more complex dynamical interpretation, however, possibly associated with barotropic instability of the compact vortex core.

This contrasts with the SPV, where $c(\widetilde{K_E, K_Z})(m, \phi)$ is distributed more broadly in latitude with systematic structure that is dominated by $m \geq 2$ (especially $m = 2$ and $m = 4$ with 2° of the pole) without much of a contribution from $m = 1$ (see Fig. 9(d)). Such a predominance of $m = 2$ is consistent with the elliptical appearance of the SPV in some images (e.g. see Figure 13).

The pattern of $c(\widetilde{K_E, K_Z})(m, \phi)$ with latitude seems consistent with an acceleration of the axisymmetric vortex core within 2° of the pole from $m = 2$ and other even numbered harmonics, possibly suggestive of an acceleration of the vortex as an elliptical perturbation of the vortex decays. At lower latitudes the pattern is indicative of a tendency to flatten the outer zonal flow profile and displace a secondary peak in $\overline{u}$ at around 86°S equatorwards. Finally, $c(\widetilde{K_E, K_Z})(m, \phi)$ in the SPJ (see Fig. 9(c)) shows a systematic pattern of zonal flow acceleration from a wide range of zonal wavenumbers near the jet core, with weak deceleration on either side, mainly dominated by low wavenumbers $m \leq 10$. This pattern indicates a similar trend to the NPJ, tending to sharpen the jet

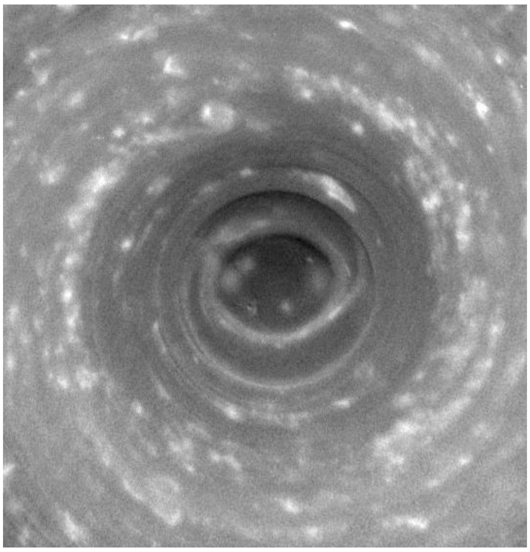

Figure 13: Image of the core of Saturn's South Polar Vortex, obtained by the Cassini ISS wide-angle camera using a spectral filter sensitive to wavelengths of infrared light centered at 752 nm on 11 October 2006. Image scale is about 17 km per pixel. Image credit from NASA/JPL/Space Science Institute, image no. PIA08332.

and strengthen its core, but with contributions spread across a wide range of m extending almost up to the resolution limit around $m = 40$.

Integrating $c(\widetilde{K_E, K_Z})(m, \phi)$ in latitude provides a determination of the overall contribution of each zonal wavenumber component to the generation of the kinetic energy of the zonal jet flow. Figure 14 shows results obtained from area-weighted integrals of $c(\widetilde{K_E, K_Z})(m, \phi)$ over the interval in latitude within $\pm 5°$ of the NPJ and SPJ respectively. This shows the clear dominance of $m = 6$ in the north in transferring kinetic energy into the NPJ (Fig. 14(b)) at a rate that is more than three times the mean conversion rate for the whole planet. $C(\widetilde{K_E, K_Z})(m)$ is also positive for many other wavenumbers, though at a much lower level. Only $m = 1, 3$ and 4 seem to show a negative conversion rate in the NPJ region, indicating that they are gaining KE at the expense of the $m = 0$ zonal jet, although this might also reflect the impact of some large scale sampling errors. In the SPJ (Fig. 14(a)), the contributions of individual wavenumber components are all relatively small in magnitude ($< 2 - 3 \times 10^{-5}$ W kg^{-1} per wavenumber) though predominantly positive except at $m = 1, 2, 4, 5$ and 13. However, none of these components feature particularly strongly in the zonal KE spectrum for the southern polar region (cf Fig. 8(a)).

$C(\widetilde{K_E, K_Z})(m)$ for the polar vortices shows a more complex and diverse situation between north and south. The SPV (Fig. 14(c)) shows strong contributions to $C(\widetilde{K_E, K_Z})(m)$ at $m = 2$ and $m = 4$, as remarked above, with only weak and probably insignficant contributions from other wavenumbers. For the NPV, however, Fig. 14(d) suggests that low wavenumber structures ($m \leq 4$) are drawing energy from the axisymmetric vortex while higher wavenumbers ($m \gtrsim 4$) are weakly feeding energy into the axisymmetric circumpolar jet surrounding the vortex, which error estimates suggest may be statistically significant unless measurement errors are heavily dominated by large scale sampling issues. This contrasting behaviour between different wavenumber ranges may go

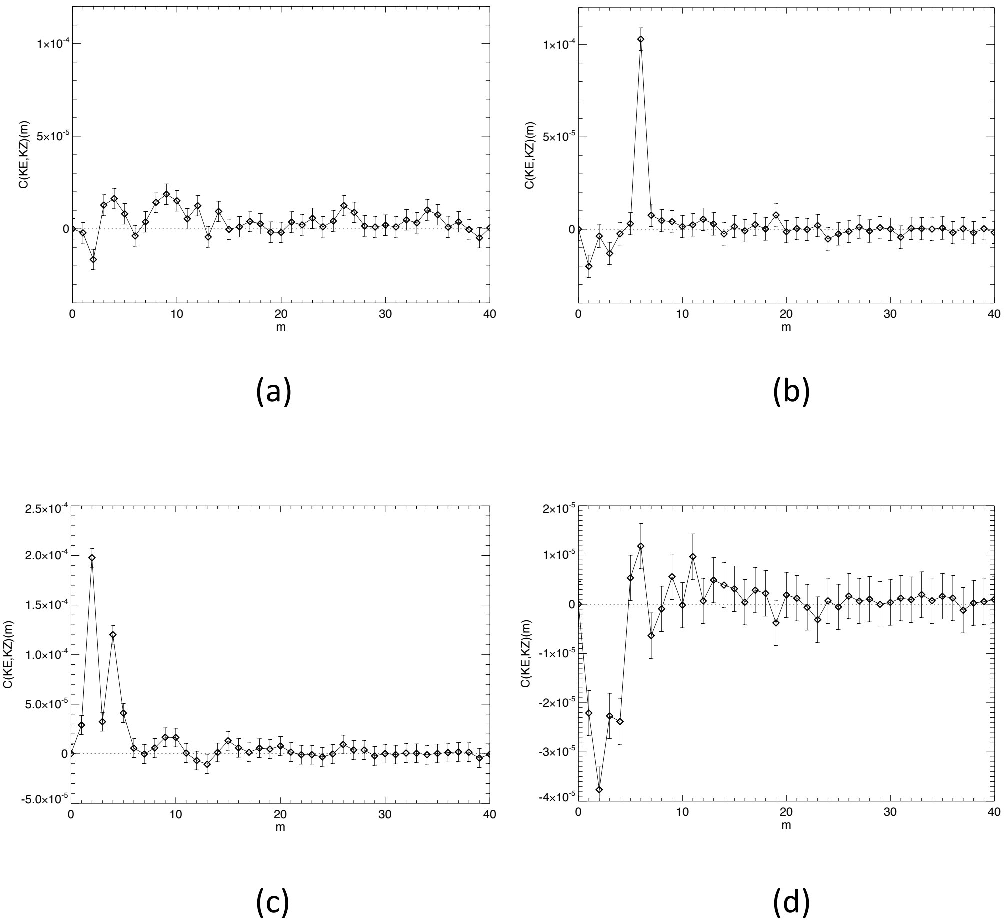

Figure 14: Spectrally resolved, eddy-zonal flow KE conversion rate, C(KE,KZ)(m) vs zonal wavenumber m for (a) Saturn's south polar jet (66°–76°S), (b) its north polar jet (70°–79°N), (c) the south polar vortex (80°–90°S) and (d) the north polar vortex (80°–90°N).

some way to explaining the apparently large statistical error in $C(K_E, K_Z)$ for the NPV (see Table 1).

5 Discussion

In this study we have analysed the velocity fields in Saturn's polar regions, as derived by Antuñano et al. (2015), to evaluate the interactions between nonaxiymmetric eddies, waves and zonal jet flows. The results show that, with the exception of the vortices immediately encircling the poles, the overall tendency is for eddies to transfer kinetic energy into the zonal jets via horizontal Reynolds stresses at a rate that is similar to the rest of Saturn's atmosphere at latitudes equatorwards of 60° (Del Genio et al., 2007; Del Genio & Barbara, 2012; Cabanes et al., 2020). This tendency would therefore seem to be confirmed in the atmospheres of both Saturn and Jupiter, at least at the level of the cloud tops of both planets. The earlier analysis of Antuñano et al. (2015) was unable to reach a conclusion concerning the sense of KE transfers between eddies and the zonal mean jets in the vicinity of the NPJ and SPJ because of excessive noise and scatter in plots equivalent to Fig.S5. They only considered a rather narrower latitude band than was analysed in Section 3.1 above, however, based on the raw, irregularly spaced velocity measurements. It may also be significant that their analysis defined u' and v' for the NPH as residuals following subtraction of a hexagonally meandering zonal jet rather than the conventional zonal mean $\overline{u}$ used here. In the present analysis, some smoothing in latitude was also applied to take account of the effective resolution of the image correlation algorithm, which also may have improved the signal-to-noise ratio of the measurements, especially in the zonal mean. As a result, the statistical analysis in Section 3.1 clearly demonstrated a statistically significant correlation consistent with a positive contribution to $C(K_E, K_Z)$.

Perhaps the most striking result of the present analysis concerns the role of the North Polar Hexagon wave in the zonal kinetic energy budget. Through our zonal spectral decomposition, it seems quite clear that the $m = 6$ hexagon wave was directly transferring KE into the zonal mean NPJ at a rate approaching 200 μW kg^{-1}. Unless this time period represents an unusual transient interval, therefore, when the NPH meanders happened to be decaying and giving up their KE to the zonal mean NPJ, this indicates that the NPH meanders were not being maintained as an active barotropic instability of the NPJ, at least at the time of the observations. If this were to be confirmed at other times, this would raise some significant questions that would need to be addressed by a whole class of explanations for the origin and maintenance of the NPH, including several recent numerical models and laboratory analogues (e.g. Aguiar et al., 2010; Morales-Juberías et al., 2011, 2015; Farrell & Ioannou, 2017; Rostami et al., 2017). Our Fig. 14(b), for example, is directly comparable with Fig. 4 of Farrell & Ioannou (2017) and shows the direct opposite of the $m = 6$ conversion rate obtained in their model. It is not clear whether our result is also inconsistent with the deep convection models of Yadav & Bloxham (2020) or Garcia et al. (2020) since they do not report on calculations of eddy-zonal flow energetics in their papers, although the zonal jets produced in such models seem strongly barotropic in character. This would certainly be of interest to calculate in further modelling studies. A key goal for the future, however, should be to measure $C(K_E, K_Z)$ for the NPH at other times to determine whether our results represent a transient phenomenon or the normal, equilibrated state of this feature of Saturn's atmosphere.

If our measurement does not represent a transient, however, then an alternative possibility that could be consistent with the results presented here is that an active baroclinic instability may be responsible for generating the $m = 6$ meanders in the NPJ. Several previous studies have shown that baroclinic instabilities can also develop into equilibrated polygonal meanders in a vertically sheared zonal jet (e.g. Hide & Mason, 1975; Bastin & Read, 1997, 1998; Sutyrin et al., 2001; Morales-Juberías et al., 2015). In the presence of a β-effect, this can lead to kinetic energy transfers from the eddies to the zonal flow, especially if the jet width is broader than the local baroclinic Rossby radius (Held & Andrews, 1983). Conclusive confirmation of this interpretation, however, would require explicit diagnosis of the baroclinic conversion rate from potential to eddy kinetic energy, involving both the large-scale vertical velocity and temperature perturbations beneath the visible cloud tops. These are not available directly in observations, and may not be feasible to obtain for the foreseeable future. There is, however, some hint of a possible reversal of the northward PV gradient with altitude close to the NPJ around the level of the cloud tops at the time of these observations in the work of Antuñano et al. (2018) that might be suggestive of baroclinic processes. One of the model simulations of Morales-Juberías et al. (2015) that reproduced a stable, hexagonal meandering jet in a shallow domain with vertical shear was also interpreted as a possible baroclinic instability, although this was not confirmed directly in other diagnostics.

The general tendency for $C(\widetilde{K_E, K_Z})(m)$ to be positive for most values of m in both the NPJ and SPJ would seem to suggest that both jets could be weakly baroclinically unstable, allowing a statistically steady trickle of KE into their parent jets via conversion from available potential energy associated with horizontal temperature gradients around and below the visible cloud tops. If this was confirmed, it would suggest an analogy between both the NPJ and SPJ and the so-called Ribbon Wave at 47° N on Saturn (e.g. Godfrey & Moore, 1986; Sayanagi et al., 2010; Gunnarson et al., 2018). The reason why the NPJ develops and maintains a strong $m = 6$ wave while the SPJ does not, however, remains somewhat mysterious and may require further observations and theoretical modelling, especially perhaps with regard to the structure of the flow beneath the visible cloud tops. Such a distinction has remained elusive to most models so far, including both shallow and deep convection scenarios.

As remarked previously, the polar vortices on Saturn are distinct structures with a closed, cyclonic circulation centred quite closely on each pole (Sánchez-Lavega et al., 2006; Sayanagi et al., 2017). Images from Cassini have shown significant non-axisymmetric perturbations to both vortices in the form of waves and smaller sub-vortices (Sánchez-Lavega et al., 2006; Dyudina et al., 2008, 2009; Baines et al., 2009). The SPV in particular was seen with an elliptical ($m = 2$) distortion in the eye wall (see Fig. 13) while both the NPV and SPV exhibited spiral cloud features in their outer regions. The NPV also contained much smaller sub-mesoscale vortices embedded within the spiral cloud bands indicating some complex local instabilities. It is noteworthy that our calculations of $c(\widetilde{K_E, K_Z})(m, \phi)$ show a strong positive signal at $m = 2$ and 4 close to the south pole, consistent with the elliptical distortion of the vortex in the visible images. This would suggest that the elliptical perturbation to the vortex was actually contributing to strengthening the polar vortex itself close to its core, although further out from the core the contribution to $C(\widetilde{K_E, K_Z})(m, \phi)$ seems consistent with $m = 2$ and 4 eddies weakly forcing a secondary jet at $\sim$ 86°S northwards. In the NPV, however, $m = 2$ appears to be making a weak negative contribution to $c(\widetilde{K_E, K_Z})(m, \phi)$, suggestive of its tendency to grow at the expense of the axisymmetric vortex and consistent with a barotropic shear instability, although the contribution of $m = 1$ is positive. This should perhaps be examined more closely in future work.

Similarities between both polar vortices and terrestrial tropical cyclones have been noted previously e.g. by Dyudina et al. (2009), who also point out the presence of many small anticyclones surrounding and embedded within Saturn's SPV. Tropical cyclones on Earth are often observed to develop non-axisymmetric perturbations to their cores and eye walls (e.g. Schubert et al., 1999; Reasor et al., 2000; Kossin & Schubert, 2001; Kossin et al., 2002), mainly due to local transient barotropic shear instabilities, although they quickly break up and disperse on timescales of a few hours. Similar perturbations are seen in Venus's polar vortices (e.g. Limaye et al., 2009), which also show some resemblance to terrestrial tropical cyclone mesovortices. The perturbations to the Venus polar vortex appear also to be due to barotropic (and baroclinic?) shear instabilities (Limaye et al., 2009) which are strongly ageostrophic, much like in terrestrial cyclones where typical Rossby numbers $Ro = U/fL \sim \zeta/f$ (where ζ is the local relative vorticity) are much greater than unity. For the Saturn polar vortices, Ro is typical O(1) (Dyudina et al., 2009; Antuñano et al., 2015; Sayanagi et al., 2017), suggesting planetary rotation may be somewhat more significant for their dynamical stability. As with other atmospheric features, their origin and depth of penetration into Saturn's deep interior remain highly uncertain (cf Garcia et al., 2020). But our overall result that $C(K_E, K_Z) \lesssim 0$ for the NPV (see Table 1) may be consistent with a weakly barotropically unstable vortex at the time of the Cassini measurements. It is likely that such instabilities are, like their terrestrial counterparts, dynamically active and transient, so it would be of significant interest, to analyse cloud motions around these features at other times to obtain more statistics on the occurrence and evolution of these unstable vortices.

Finally, we note that, given the high quality of images available from spacecraft such as Cassini, it would be desirable in future to take even fuller account of the potential sources of uncertainty in velocity measurements than has been possible in this study. In particular, our treatment of navigation errors here was relatively simple and straightforward, because foreshortening effects and other anisotropies were relatively small. But in general such errors may be strongly anisotropic and inhomogeneous across an image, for which the development of better methods may be desirable to quantify such uncertainties properly.

Acknowledgments

We are grateful to three anonymous reviewers for their careful reading of this manuscript and their constructive comments. PLR and GC were funded by the UK Science and Technology Facilities Council (ST/N00082X/1 and ST/S000461/1). TdR and ASL were supported by the Spanish project PID2019-109467GB-I00 (MINECO/FEDER, UE) and Grupos Gobierno Vasco IT1366-19. AA was supported by a European Research Council Consolidator Grant under the European Union's Horizon 2020 research innovation programme, grant agreement number 723890, at the University of Leicester, and by the Spanish Juan de la Cierva-Incorporacion programme, grant agreement number IJC2019-040328-I/AEI/10.13039/501100011033. Gridded velocity measurements from this study are available via the University of Oxford Research Archive (Antuñano et al., 2021).

References

Aguiar, A. C. B., Read, P. L., Wordsworth, R. D., Salter, T., & Yamazaki, Y. H. (2010). A laboratory model of Saturn's North Polar Hexagon. *Icarus*, *206*, 755–763.

Allison, M., Godfrey, D. A., & Beebe, R. F. (1990). A wave dynamical interpretation of Saturn's polar hexagon. *Science*, *247*, 1061–1063.

Andrews, D. G., Holton, J. R., & Leovy, C. B. (1987). *Middle atmosphere dynamics.* Orlando, Fl: Academic Press.

Antuñano, A., del Río-Gaztelurrutia, T., Hueso, R., Read, P. L., & Sánchez-Lavega, A. (2021). Cassini Saturn polar velocity fields. *University of Oxford Research Archive*, *v.1*, [Dataset]. Retrieved from `https://doi.org/10.5287/bodleian:X5dOD7ePD`

Antuñano, A., del Río-Gaztelurrutia, T., Sánchez-Lavega, A., & Hueso, R. (2015). Dynamics of Saturn's polar regions. *J. Geophys. Res.: Planets*, *120*, 155–176. doi: 10.1002/2014JE004709

Antuñano, A., del Río-Gaztelurrutia, T., Sánchez-Lavega, A., Read, P. L., & Fletcher, L. N. (2018). Potential vorticity of Saturn's polar regions: Seasonality and instabilities. *J. Geophys. Res.: Planets*, *124*, 186–201. doi: 10.1029/2018JE005764

Archinal, B. A., & et al. (2018). Report of the IAU working group on cartographic coordinates and rotation elements: 2015. *Celest. Mech. Dyn. Astr.*, *130*, 22.

Baines, K. H., Momary, T. W., Fletcher, L. N., Showman, A. P., Roos-Serote, M., Brown, R. H., ... Nicholson, P. D. (2009). Saturn's north polar cyclone and hexagon at depth revealed by Cassini/VIMS. *Plan. Space Sci.*, *57*, 1671–1681.

Barber, C. B., Dobkin, D. P., & Huhdanpaa, H. (1996). The Quickhull algorithm for convex hulls. *ACM Trans. Math. Software*, *22*, 469–483.

Bastin, M., & Read, P. L. (1997). A laboratory study of baroclinic waves and turbulence in an internally heated rotating fluid annulus with sloping endwalls. *J. Fluid Mech.*, *339*, 173–198.

Bastin, M., & Read, P. L. (1998). Experiments on the structure of baroclinic waves and zonal jets in an internally heated rotating cylinder of fluid. *Phys. Fluids*, *10*, 374–389.

Boffetta, G., De Lillo, F., Mazzino, A., & Musacchio, S. (2011). A flux loop mechanism in two-dimensional stratified turbulence. *EPL*, *95*, 34001. doi: 10.1209/0295-5075/95/34001

Cabanes, S., Espa, S., Galperin, B., Young, R. M. B., & Read, P. L. (2020). Revealing the intensity of turbulent energy transfer in planetary atmospheres. *Geophys. Res. Lett.*, *47*, e2020GL088685. doi: 10.1029/2020GL088685

Chemke, R., & Kaspi, Y. (2015). The latitudinal dependence of atmospheric jet scales and macroturbulent energy cascades. *J. Atmos. Sci.*, *72*, 3891–3907. doi: 10.1175/JAS-D-15-0007.1

Del Genio, A. D., & Barbara, J. M. (2012). Constraints on saturn's tropospheric general circulation Cassini ISS images. *Icarus*, *219*, 689–700.

Del Genio, A. D., Barbara, J. M., Ferrier, J., Ingersoll, A. P., West, R. A., Vasavada, A. R., ... Porco, C. C. (2007). Saturn eddy momentum fluxes and convection: First estimates from Cassini images. *Icarus*, *189*, 479–492.

Desch, M. D., & Kaiser, L. M. (1981). Voyager measurements of the rotation period of Saturn's magnetic field. *Geophys. Res. Lett.*, *8*, 253–256. doi: 10.1029/GL008i003p00253

Dyudina, U. A., Ingersoll, A., Ewald, S., Vasavada, A., West, R., Del Genio, A., ... Fletcher, L. (2008). Dynamics of saturn's south polar vortex. *Science*, *319*, 1801.

Dyudina, U. A., Ingersoll, A. P., Ewald, S. P., Vasavada, A. R., West, R. A., Baines, K. H., ... Fletcher, L. N. (2009). Saturn's south polar vortex compared to other large vortices in the solar system. *Icarus*, *202*, 240–248. doi: 10.1016/j.icarus.2009.02.014

Farrell, B. F., & Ioannou, P. J. (2017). Statistical state dynamics based theory for the formation and equilibration of Saturn's north polar jet. *Phys. Rev. Fluids*, *2*, 073801. doi: 10.1103/PhysRevFluids.2.073801

Fletcher, L. N., Orton, G. S., Sinclair, J. A., Guerlet, S., Read, P. L., Antuñano, A., ... Calcutt, S. B. (2018). A hexagon in saturn's northern stratosphere surrounding the emerging summertime polar vortex. *Nature Comms.*, *9*, 3564. doi: 10.1038/s41467-018-06017-3

Früh, W.-G., & Read, P. L. (1999). Experiments on a barotropic rotating shear layer. Part 1. instability and steady vortices. *J. Fluid Mech.*, *383*, 143–173.

Garcia, F., Chambers, F. R. N., & Watts, A. L. (2020). Deep model simulation of polar vortices in gas giant atmospheres. *Mon. Not. R. Astr. Soc.*, *499*, 4698–4715. doi: 10.1093/mnras/staa2962

Godfrey, D. A. (1988). A hexagonal feature around Saturn's north pole. *Icarus*, *76*, 335–356.

Godfrey, D. A., & Moore, V. (1986). The Saturnian Ribbon feature - a baroclinically unstable model. *Icarus*, *68*, 313–343.

Gunnarson, J. L., Sayanagi, K. M., Blalock, J. J., Fletcher, L. N., Ingersoll, A. P., Dyudina, U. A., ... Draham, R. L. (2018). Saturn's New Ribbons: Cassini observations of planetarywaves in Saturn's 42°N atmospheric jet. *Geophys. Res. Lett.*, *45*, 7399–7408. doi: 10.1029/2018GL078156

Held, I. M., & Andrews, D. G. (1983). On the direction of the eddy momentum flux in baroclinic instability. *J. Atmos. Sci.*, *40*, 2220–2231.

Hide, R., & Mason, P. J. (1975). Sloping convection in a rotating fluid. *Adv. in Phys.*, *24*, 47–100.

Hueso, R., Legarreta, J., García-Melendo, E., Sánchez-Lavega, A., & Pérez-Hoyos, S. (2009). The Jovian anticyclone BA: ii. circulation and models of its interaction with the zonal jets. *Icarus*, *203*, 499–515.

Ingersoll, A. P., Beebe, R. F., Mitchell, J. L., Garneau, G. W., Yagi, G. M., & Müller, J.-P. (1981). Interaction of eddies and mean zonal flow on Jupiter as inferred from Voyager 1 and 2 images. *J. Geophys. Res.*, *86*, 8733–8743. doi: 10.1029/JA086iA10p08733

Kossin, J. P., McNoldy, B. D., & Schubert, W. H. (2002). Vortical swirls in hurricane eye clouds. *Mon. Weather Rev.*, *130*, 3144–3149.

Kossin, J. P., & Schubert, W. H. (2001). Mesovortices, polygonal flow patterns, and rapid pressure falls in hurricane-like vortices. *J. Atmos. Sci.*, *58*, 2196–2209.

Limaye, S. S., Kossin, J. P., Rozoff, C., Piccioni, G., Titov, D. V., & Markiewicz, W. J. (2009). Vortex circulation on Venus: dynamical similarities with terrestrial hurricanes. *Geophys. Res. Lett.*, *36*, L04204. doi: 10.1029/2008GL036093

Liu, T., Sayanagi, K. M., Brueshaber, S. R., Blalock, J. J., Ingersoll, A. P., Dyudina, U. A., & Ewald, S. P. (2019). Saturn's North Polar Vortex structure extracted from cloud images by the optical flow method. *J. Geophys. Res.: Planets*, *124*, 3041–3062. doi: 10.1029/2019JE005974

Montgomery, M. T., & Smith, R. K. (2017). Recent developments in the fluid dynamics of tropical cyclones. *Ann. Rev. Fluid Mech.*, *49*, 541–574. doi: 10.1146/annurev-fluid-010816-060022

Morales-Juberías, R., Sayanagi, K., Dowling, T. E., & Ingersoll, A. P. (2011). Emergence of polar-jet polygons from jet instabilities in a Saturn model. *Icarus*, *211*, 1284. doi: 10.1016/j.icarus.2010.11.006

Morales-Juberías, R., Sayanagi, K. M., Simon, A. A., Fletcher, L. N., & Cosentino, R. G. (2015). Meandering shallow atmospheric jet as a model of Saturn's north-polar hexagon. *Astrophys. J. Lett.*, *806*, L18. doi: 10.1088/2041-8205/806/1/L18

O'Neill, M. E., Emanuel, K. A., & Flierl, G. R. (2015). Polar vortex formation in giant-planet atmospheres due to moist convection. *Nature Geosci.*, *8*, 523–526. doi: 10.1038/NGEO2459

O'Neill, M. E., Emanuel, K. A., & Flierl, G. R. (2016). Weak jets and strong cyclones: Shallow-water modeling of giant planet polar caps. *J. Atmos. Sci.*, *73*, 1841–1855. doi: 10.1175/JAS-D-15-0314.1

Peixóto, J. P., & Oort, A. H. (1974). The annual distribution of atmospheric energy on a planetary scale. *J. Geophys. Res.*, *79*, 2149–2159.

Read, P. L., Conrath, B. J., Fletcher, L. N., Gierasch, P. J., Simon-Miller, A. A., & Zuchowski, L. C. (2009). Mapping potential vorticity dynamics on Saturn: zonal mean circulation from Cassini and Voyager data. *Plan. Space Sci.*, *57*, 1682–1698. doi: 10.1016/j.pss.2009.03.004

Reasor, P. D., Montgomery, M. T., Marks, F. D., & Gamache, J. F. (2000). Low-wavenumber structure and evolution of the hurricane inner core observed by airborne dual-Doppler radar. *Mon. Weather Rev.*, *128*, 1653–1680.

Rostami, M., Zeitlin, V., & Spiga, A. (2017). On the dynamical nature of Saturn's North Polar hexagon. *Icarus*, *297*, 59–70. doi: 10.1016/j.icarus.2017.06.006

Salyk, C., Ingersoll, A. P., Lorre, J., Vasavada, A., & Del Genio, A. D. (2006). Interaction between eddies and mean flow in Jupiter's atmosphere: Analysis of Cassini imaging data. *Icarus*, *185*, 430–442. doi: 10.1016/j.icarus.2006.08.007

Sánchez-Lavega, A., del Río-Gaztelurrutia, T., Hueso, R., Příez-Hoyos, S., García-

Melendo, E., Antuñano, A., . . . Wesley, A. (2014). The long-term steady motion of Saturn's hexagon and the stability of its enclosed jet stream under seasonal changes. *Geophys. Res. Lett.*, *41*, 1425–1431. doi: 10.1002/2013GL059078.

Sánchez-Lavega, A., Hueso, R., Pérez-Hoyos, S., & Rojas, J. F. (2006). A strong vortex in Saturn's south pole. *Icarus*, *184*, 524–531. doi: 10.1016/j.icarus.2006.05.020

Sánchez-Lavega, A., Pérez-Hoyos, S., Acarreta, J. R., & French, R. G. (2002). No hexagonal wave around Saturn's southern pole. *Icarus*, *160*, 216–219.

Sánchez-Lavega, A., Rojas, J. F., Acarreta, J. R., Lecacheux, J., Colas, F., & Sada, P. V. (1997). New observations and studies of Saturn's long-lived north polar spot. *Icarus*, *128*, 322–334.

Sayanagi, K. M., Baines, K. H., Dyudina, U. A., Fletcher, L. N., Sánchez-Lavega, A., & West, R. A. (2018). Saturn's polar atmosphere. In K. H. Baines, F. M. Flasar, N. Krupp, & T. E. Stallard (Eds.), *Saturn in the 21st century* (p. 337–376). Cambridge University Press. doi: 10.1017/9781316227220.012

Sayanagi, K. M., Blalock, J. J., Dyudina, U. A., Ewald, S. P., & Ingersoll, A. P. (2017). Cassini ISS observation of Saturn's north polar vortex and comparison to the south polar vortex. *Icarus*, *285*, 68–82. doi: 10.1016/j.icarus.2016.12.011

Sayanagi, K. M., Morales-Juberias, R., & Ingersoll, A. P. (2010). Saturn's Northern Hemisphere Ribbon: simulations and comparison with the meandering Gulf Stream. *J. Atmos. Sci.*, *67*, 2658–2678. doi: 10.1175/2010JAS3315.1

Schubert, W. H., Montgomery, M. T., Taft, R. K., Guinn, T. A., Fulton, S. R., Kossin, J. P., & Edwards, J. P. (1999). Polygonal eyewalls, asymmetric eye contraction, and potential vorticity mixing in hurricanes. *J. Atmos. Sci.*, *56*, 1197–1223.

Seidelmann, P. K., Archinal, B. A., A'hearn, M. F., Conrad, A., Consolmagno, G. J., Hestroffer, D., . . . Williams, I. P. (2007). Report of the IAU/IAG working group on cartographic coordinates and rotational elements. *Celestial Mech. Dyn. Astron*, *98*, 155–180. doi: 10.1007/s10569-007-9072-y

Sommeria, J., Meyers, S., & Swinney, H. (1989). Laboratory model of a planetary eastward jet. *Nature*, *337*, 58–61.

Sommeria, J., Meyers, S. D., & Swinney, H. L. (1991). Experiments on vortices and Rossby waves in eastward and westward jets. In A. R. Osborne (Ed.), *Nonlinear topics in ocean physics* (pp. 227–269). Amsterdam: North Holland.

Sromovsky, L., Revercomb, H., Suomi, V., Limaye, S., & Krauss, R. (1982). Jovian winds from Voyager 2. Part II: analysis of eddy transports. *J. Atmos. Sci.*, *39*, 1413–1432.

Sutyrin, G., Ginis, G. I., & Frolov, S. A. (2001). Equilibration of baroclinic meanders and deep eddies in a Gulf Stream-type jet over a sloping bottom. *J. Phys. Oceanogr.*, *31*, 2049–2065.

Sánchez-Lavega, A., Sromovsky, L. A., Showman, A. P., Del Genio, A. D., Young, R. M. B., Hueso, R., . . . Barbara, J. M. (2019). Gas giants. In B. Galperin & P. L. Read (Eds.), *Zonal jets: Phenomenology, genesis and physics* (pp. 72–103). Cambridge, UK: Cambridge University Press.

Vallis, G. K. (2017). *Atmospheric and oceanic fluid dynamics - fundamentals and large-scale circulation (2nd edition).* Cambridge, UK: Cambridge University Press.

Vasavada, A. R., & Showman, A. P. (2005). Jovian atmospheric dynamics: an update after Galileo and Cassini. *Rep. Prog. Phys.*, *68*, 1935–1996. doi: 10.1088/0034-4885/68/8/R06

Yadav, R. K., & Bloxham, J. (2020). Deep rotating convection generates the polar hexagon on Saturn. *PNAS*, *117*, 13991–13996. doi: 10.1073/pnas.2000317117

Supporting Information for “Energy exchanges in Saturn’s polar regions from Cassini observations: Eddy-zonal flow interactions”

Peter L. Read[1], Arrate Antuñano[2], Simon Cabanes[3], Greg Colyer[1],

Teresa del Río Gaztelurrutia[2], and Agustin Sanchez-Lavega[2]

[1]Atmospheric, Oceanic and Planetary Physics, Department of Physics, University of Oxford, Clarendon Laboratory, Parks Road, Oxford, OX1 3PU, UK

[2]Dpto de Física Aplicada, Escuela de Ingeniería de Bilbao, UPV/EHU, Spain

[3]DICEA, Sapienza Università di Roma, Via Eudossiana, 18 - 00184, Rome, Italy

Contents of this file

In the following section we include additional figures that supplement the information provided in the main text. Figure S1 shows the distribution in latitude and longitude of the original velocity vectors as measured by Antuñano et al. (2015). Figure S2 shows the distribution of interpolated points on regular longitude-latitude grids for each of the northern and southern hemispheres. Figure S3 presents maps of u and v for the southern hemisphere with a segment of data from longitudes 110° - 185° inserted into the data gap between 35° and 110° longitude, as an example of how this gap was filled to enable Fourier analyses of the zonal structure of the flow.

Figure S4 presents profiles in latitude of the (Pearson) correlation coefficients between u' and v' for the northern and southern hemispheres. For this calculation, data were analysed as the running mean in latitude over a 1° interval to reflect the effective resolution of the original velocity measurements.

Figure S5 shows the pointwise distribution of $\overline{u'v'}$ vs $d\overline{u}/dy = (1/a)\cos\phi d(\overline{u}/\cos\phi)/d\phi$ for (a) the vicinity of the NPJ and (b) the SPJ (±4° of the jet cores). Athough there is quite a lot of scatter among the points in both jets, even by eye there is some indication of a positive correlation between $\overline{u'v'}$ and $\partial\overline{u}/\partial y$ in both frames, consistent with a positive contribution to $C(K_E, K_Z)$. Calculation of the Pearson correlation coefficients for each of the NPJ and SPJ latitude bands with 1° latitude smoothing gives values of 0.59 and 0.40, whereas the Spearman (non-parametric) rank correlation coefficients from these data yields values of 0.47 and 0.54 respectively, indicating a rejection of the null (uncorrelated) hypothesis at the $> 99\%$ confidence level.

Figure S6 presents an alternative version of Figure 9 in the main text but using linear scales for both wavenumber and spectral energy density.

Figure S7 compares the observed structure of u and v (frames (a) and (c)) with the flow corresponding only to the $m = 0$ and $m = 6$ zonal Fourier components ((b) and (d)).

References

Antuñano, A., del Río-Gaztelurrutia, T., Sánchez-Lavega, A., & Hueso, R. (2015). Dynamics of Saturn's polar regions. *J. Geophys. Res.: Planets*, *120*, 155–176. doi: 10.1002/2014JE004709

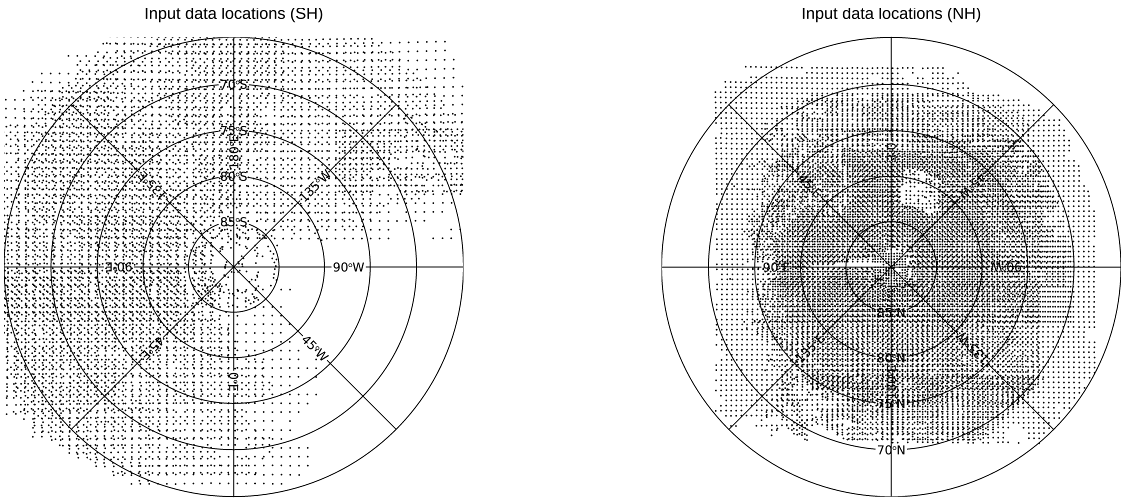

Figure S1. Locations in longitude and latitude of the original velocity vector measurements as obtained by Antuñano et al. (2015). Note that velocity vectors were not available in the south equatorwards of 76°S between longitudes of $\sim$ 35°-110°W.

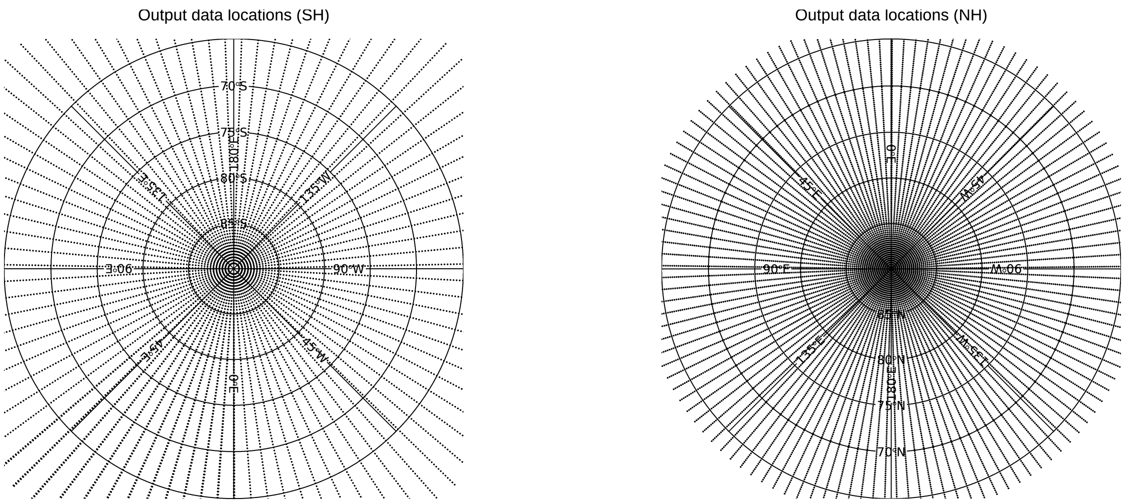

Figure S2. Locations in longitude and latitude of the velocity vector measurements as obtained by Antuñano et al. (2015) interpolated onto regular longitude-latitude grids for each hemisphere.

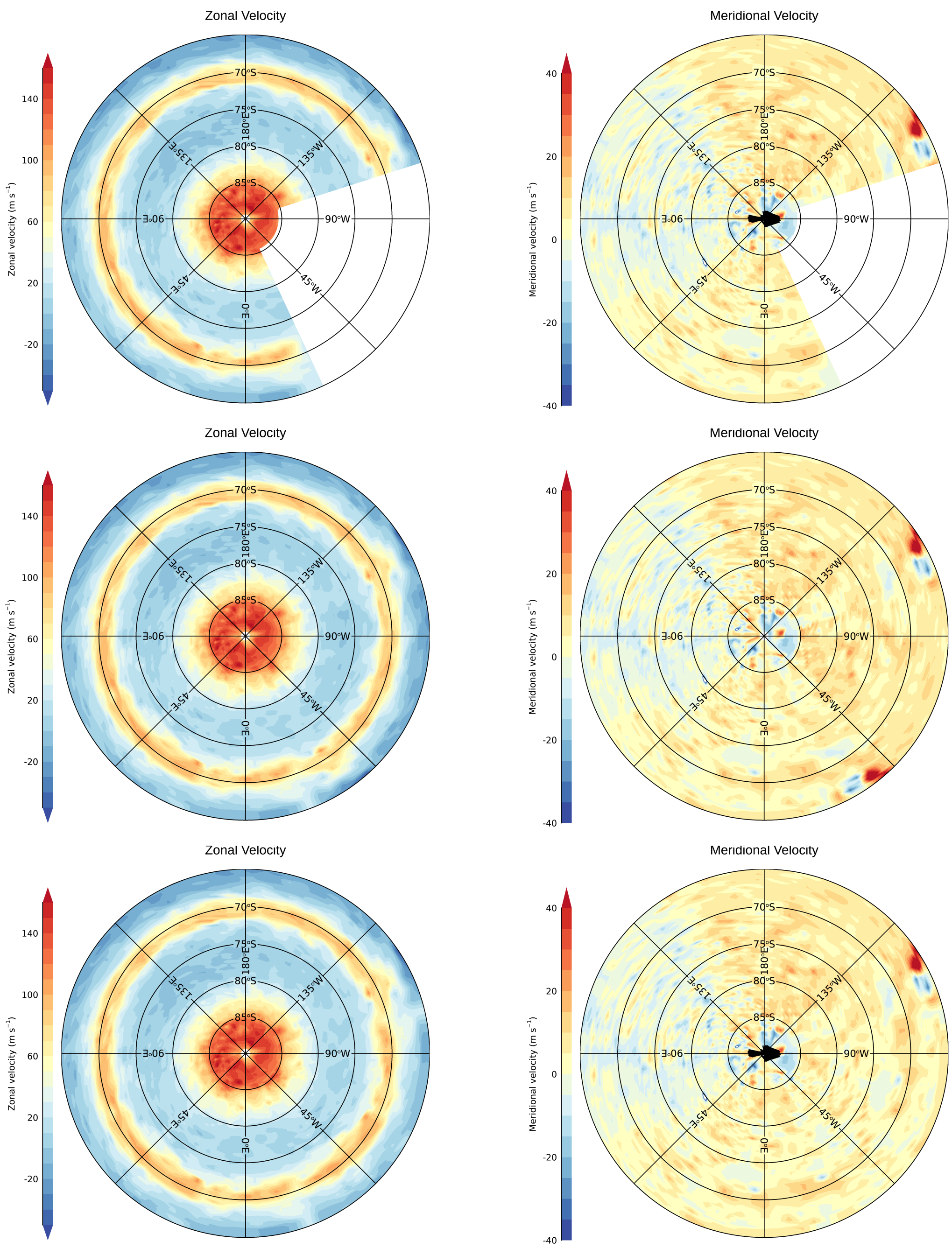

Figure S3. Cloud-top level velocity fields, obtained from cloud-tracked wind measurements using Cassini ISS images by Antuñano et al. (2015), for Saturn's (a) south polar region. As discussed in the main text, velocity vectors were not available in the south equatorwards of 76°S between longitudes of ∼ 35°-110°W, as indicated in (a) and (b). The fields shown in (c) and (d), and (e) and (f) were obtained by inserting data from longitudes 110°-185° [(c) and (d)] or 320°-35° into the data gap, to illustrate two examples of how the data gap was filled before carrying out zonal Fourier analysis.

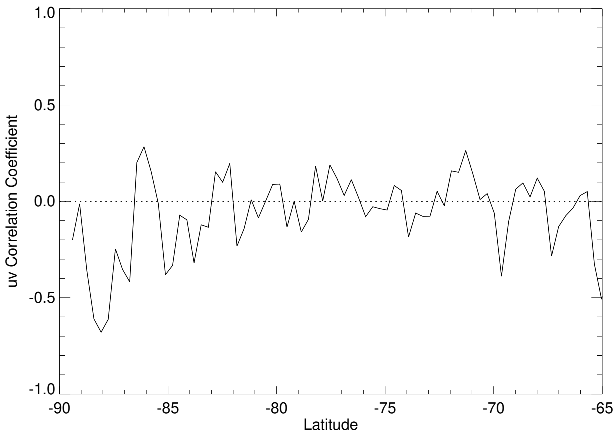

Figure S4. Profiles in latitude of the Pearson correlation coefficient between u' and v' in longitude for (a) the southern and (b) the northern hemispheres of Saturn from the data of Antuñano et al. (2015). Interpolated data were smoothed in latitude using a running mean of width 1° before computing the correlation coefficient (in longitude).

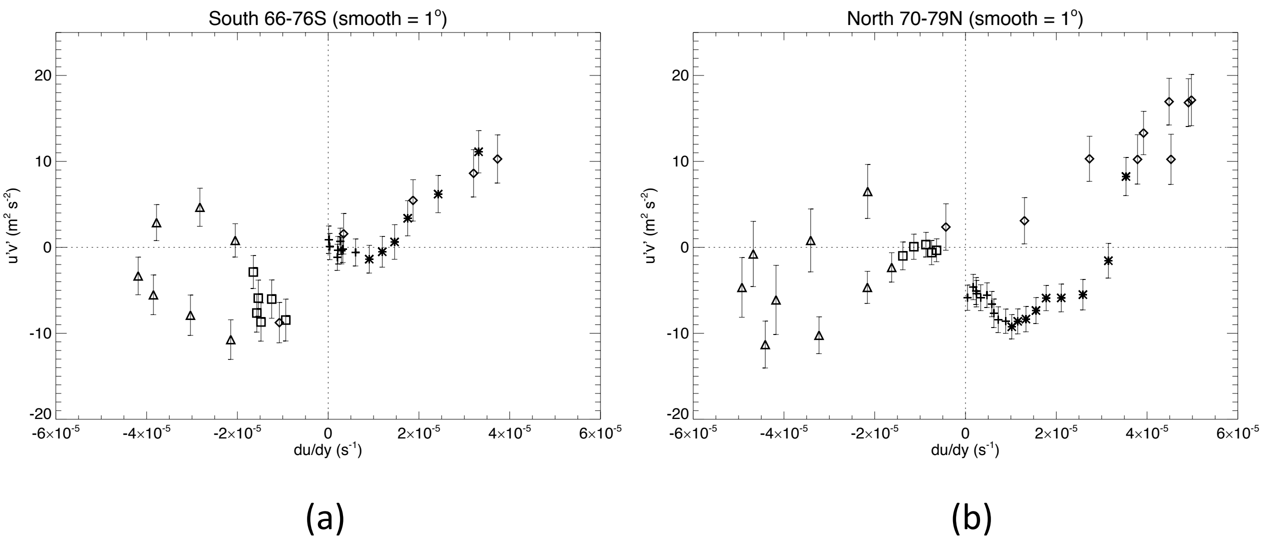

Figure S5. Pointwise scatter plots of eddy momentum flux, $\overline{u'v'}$, vs $\partial\overline{u}/\partial y$ for (a) Saturn's south polar jet region (66°-76° S) and (b) the south polar jet region (72°-80° N. Both plots use a smoothing in latitude of width $\sim 1°$. Symbols plotted indicate the latitude band from which each point is taken. For (a) squares are from 66°-68°S, triangles from 68°-70°S, diamonds from 70°-72°S, stars from 72°-74°S and crosses are from 74°-76°S. For (b), squares are from 78°-79°N, triangles from 76°-78°N, diamonds from 74°-76°N, stars from 72°-74°N and crosses are from 70°-72°N.

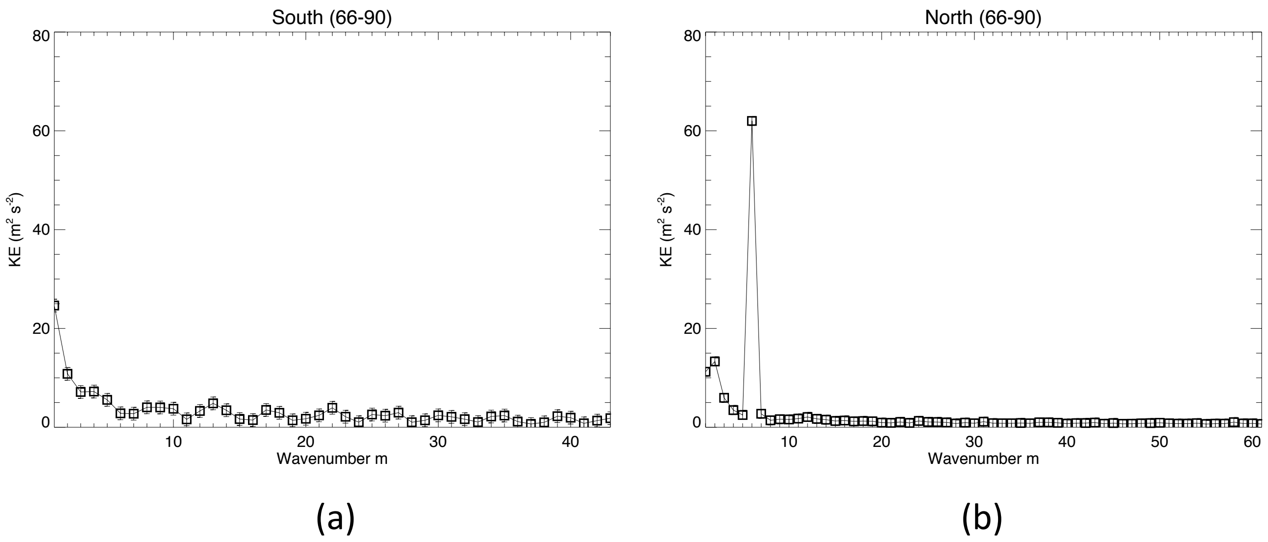

Figure S6. Area-weighted kinetic energy spectra for (a) the southern and (b) the northern polar regions (66°–90° latitude).

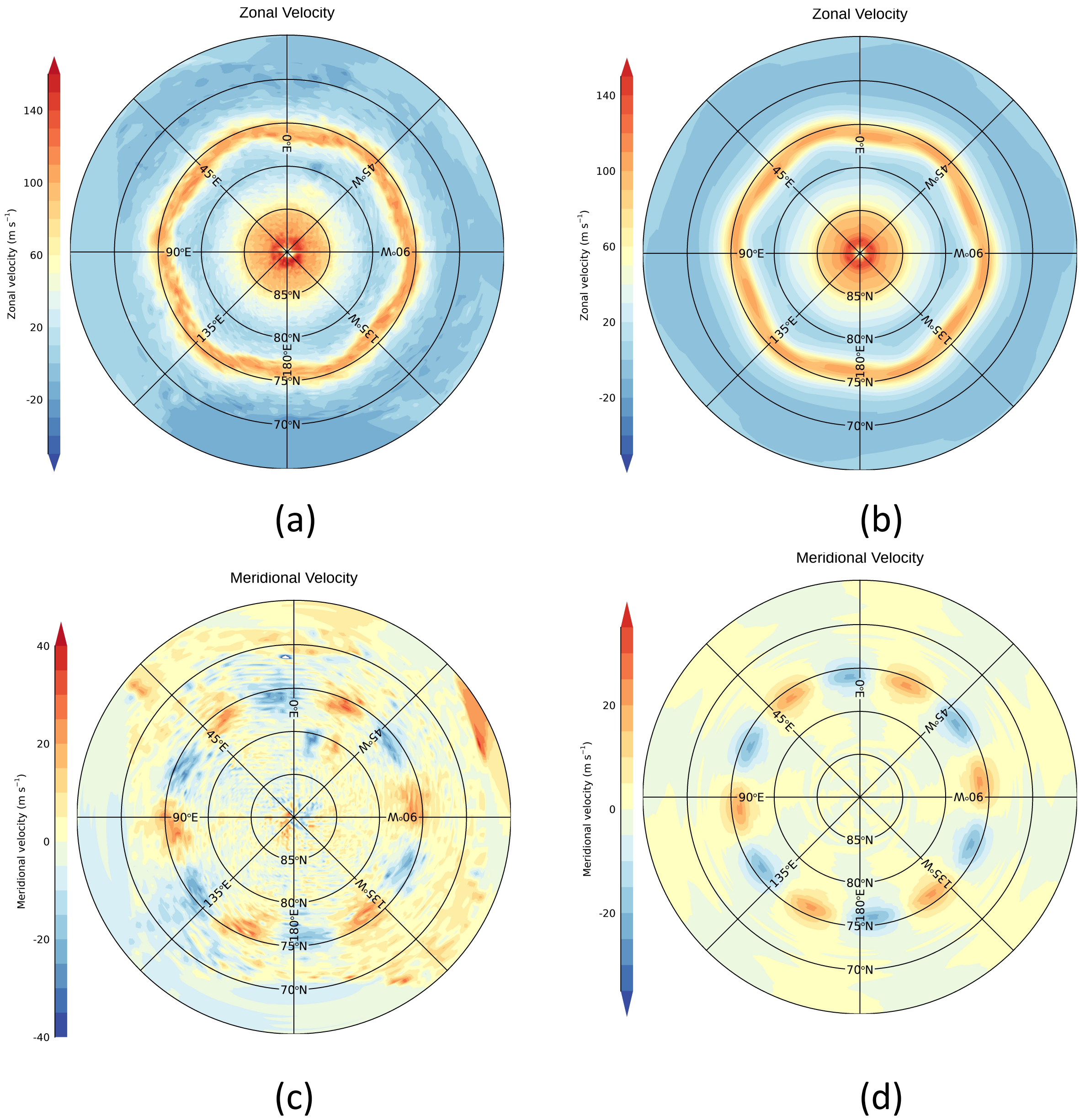

Figure S7. Comparison between the complete u and v components of the velocity field in the northern polar latitudes of Saturn ((a) and (c)), as obtained by Antuñano et al. (2015), and the contributions solely due to the $m = 0$ and $m = 6$ zonal Fourier harmonics ((b) and (d)). In the vicinity of the NPH these two harmonics capture more than 93% of the total kinetic energy.